Microscopic Investigations of Degradation in Lithium-Ion Batteries

zur Erlangung des akademischen Grades

Doktor der Ingenieurwissenschaften

der Fakultät für Maschinenbau

Karlsruher Institut für Technologie (KIT)

genehmigte

Dissertation

von

Dipl. –Ing. Di Chen

Tag der mündlichen Prüfung: 28. Juni 2012

Hauptreferent: Prof. Dr. rer. nat. Oliver Kraft

Korreferent: Prof. Dr. rer. nat. Michael J. Hoffmann

Contents

Abstract

Rechargeable batteries based on the lithium ion technology are promising candidates for future mobile and stationary energy storage. The electrodes of the batteries are the most important components which critically determine energy and power density as well as reliability. In current electrodes, sufficient ionic and electronic conductivities can only be achieved by using small active material particles. These small particles are often in the range of several hundred nanometer, which complicate detailed investigations. Typical electrochemical characterization methods can only detect average volume changes of a whole electrode. In this work, microscopic techniques were used to locally investigate reaction and degradation mechanisms on the nanometer scale. Besides conventional scanning electron microscopy (SEM), novel experimental methods were developed to observe electrode materials inside the vacuum chamber of a scanning electron microscope. An *in situ* SEM technique allows for monitoring the electrode morphology in dependence to the state of charge in real time. For long term tests that require a higher number of cycles, an *ex situ* technique was established that made it possible to observe the same location of an electrode before and after a number of cycles at a defined state of charge. Both microscopic experimental methods are helpful for investigating localized physical and chemical processes inside the lithium cells. Such knowledge is necessary for improving the reliability and increasing the energy density of lithium-ion batteries. The SEM investigations were used to reveal details of the electrochemical reactions in the conversion materials SnO_2 and $CuCr_2Se_4$. In $LiMn_{1.95}Al_{0.05}O_4$ a mechanical degradation pathway was identified. After a given number of cycles cracks appeared in the particles. A strong particle size dependence of this type of damage could be found where small particles proved to be very resistant against this damage. For very high cycle numbers, slip was detected on the electrode particles indicating the activity of dislocations in this theoretically brittle material. The dependence of the damage on the number of cycles and the particle size is suggestive of a mechanical fatigue process, which may govern degradation of such materials at high cycle numbers. In contrast to many other degradation pathways, the mechanical degradation mechanism is inevitable. Therefore it may be of importance for the reliability of real batteries at high cycle numbers.

Kurzzusammenfassung

Lithium-Ionen-Batterien sind schon heute vielfach im Einsatz und gelten als aussichtsreichste Kandidaten für zukünftige Anwendungen für die mobile und stationäre Energiespeicherung. Die Elektroden der Batterien sind dabei die wichtigsten Komponenten, und verfügen über einen entscheidenden Einfluss auf die Energie- und Leistungsdichte sowie die Zuverlässigkeit. Ausreichende ionische und elektronische Leitfähigkeiten der Elektroden können nur mit kleinen Partikeln erreicht werden, die oft Größen im Bereich von wenigen hundert Nanometern besitzen, weshalb neue Methoden zur Untersuchung von Materialveränderungen im Einsatz entwickelt werden müssen. Mit den typischen elektrochemischen Charakterisierungsmethoden können zum Beispiel nur die durchschnittlichen Volumenveränderungen einer ganzen Elektrode ermittelt werden. In dieser Arbeit wurde Elektronenmikroskopie verwendet, um die Reaktion- und Degradationsmechanismen im Nanometerbereich zu untersuchen. Um Elektrodenmaterialien in der Vakuumkammer eines Rasterelektronenmikroskops (REM) zu beobachten, wurde eine *in situ* REM-Technik entwickelt, die die Echtzeituntersuchung der Elektrodenmorphologie in Abhängigkeit vom Ladezustand ermöglicht. Für Langzeituntersuchungen, die eine hohe Zyklenzahl erfordert, wurde eine *ex situ* REM-Technik etabliert. Mit dieser Technik, ist es möglich, die Morphologie an derselben Stelle einer Elektrode vor und nach einer bestimmten Anzahl von Zyklen bei definierten Ladezuständen zu beobachten. Beide Methoden ermöglichen die lokale Untersuchung der physikalischen und chemischen Prozesse in Lithium-Zellen. Die damit gewonnenen Kenntnisse sind notwendig um die Zuverlässigkeit zu verbessern und die Energiedichte zu erhöhen. Beispielhaft wurden Details der elektrochemischen Reaktionen in den Konversionsmaterialien SnO_2 und $CuCr_2Se_4$ im *in situ* REM-Experiment untersucht. Im *ex situ* REM-Experiment, wurde eine mechanische Degradation des Interkalationsmaterials $LiMn_{1.95}Al_{0.05}O_4$ (LMAO) festgestellt. Nach der zyklischen Belastung wurden mechanische Beschädigungen in der Form von Rissen in den Partikeln nachgewiesen. Es stellte sich heraus, dass kleine Partikel im Gegensatz zu großen, sehr resistent gegenüber mechanischen Beschädigungen sind, sodass ein Größeneffekt festgestellt werden konnte. Bei hoher Zyklenzahl, weist das Auftreten von Gleitbändern an der Partikeloberfläche der Elektrode auf plastische Verformung in diesem an sich spröden Material. Die Abhängigkeit der mechanischen

Beschädigung von der Zyklenzahl und der Teilchengröße deutet auf einen mechanischen Ermüdungsprozess hin. Damit kann auf der Basis dieser Arbeit der Schluss gezogen werden, dass mechanische Ermüdung eine wesentliche Rolle für die Degradation der Elektrodenmaterialien spielt und daher maßgeblich für die Zuverlässigkeit der Batterien unter hoher zyklischer Belastung ist.

Appendix

HEV	hybrid electrical vehicles
EV	electrical vehicles
OCV	open circuit voltage
SOC	state of charge
LCO	$LiCoO_2$
LMO	$LiMn_2O_4$
LFP	$LiFePO_4$
LNO	$LiNiO_2$
LMNCO	$LiMn_{1/3}Ni_{1/3}Co_{1/3}O_2$
LNCAO	$LiNi_{0.8}Co_{0.15}Al_{0.05}O_2$
SOH	state of health
LMAO	$LiMn_{1.95}Al_{0.05}O_4$
LMNO	$LiMn_{1.5}Ni_{0.5}O_4$
LMNFO	$LiMn_{1.5}Ni_{0.4}Fe_{0.1}O_4$
K_C	fracture toughness
CCS	$CuCr_2Se_4$
EIS	electrochemical impedance spectroscopy
XRD	X-ray diffraction
SEM	scanning electron microscopy
ESEM	environmental scanning electron microscope
GCPL	galvanostatic cycling with potential limitation
IC	incremental capacities
FIB	focused ion beam
PVDF	polyvinylidene fluoride
NMP	N-methyl-2-pyrrolidone
TFSI	bis(trifluoromethanesulfonyl)imide
BMPyrr	buthylmethylpyrrolidinium
IL	ionic liquid
EC	ethylene carbonate
DMC	dimethyl carbonate
PE	polyethylene
ICA	incremental capacity analysis

1 Introduction

In the periodic table of elements, lithium is placed under hydrogen at the upper left corner. This position indicates that the lithium atom weighs only slightly more than hydrogen and helium atoms and that lithium is highly electropositive. Its atomic and ionic radii are relatively small and lithium can therefore be used to make high voltage electrochemical batteries with high specific capacity.[1] In fact, rechargeable lithium-ion batteries are advantageous compared to other battery systems due to their high specific energy, power, reversibility and low self-discharge. Figure 1 illustrates the specific energy density and volumetric energy density of several battery technologies at the cell level.[2] Both energy density values of lithium-ion batteries are almost twice as high as those of Ni-MH batteries. Due to these advantages, lithium-ion batteries have been widely used in the last two decades for example for small portable devices such as cell phones, laptops and cameras.

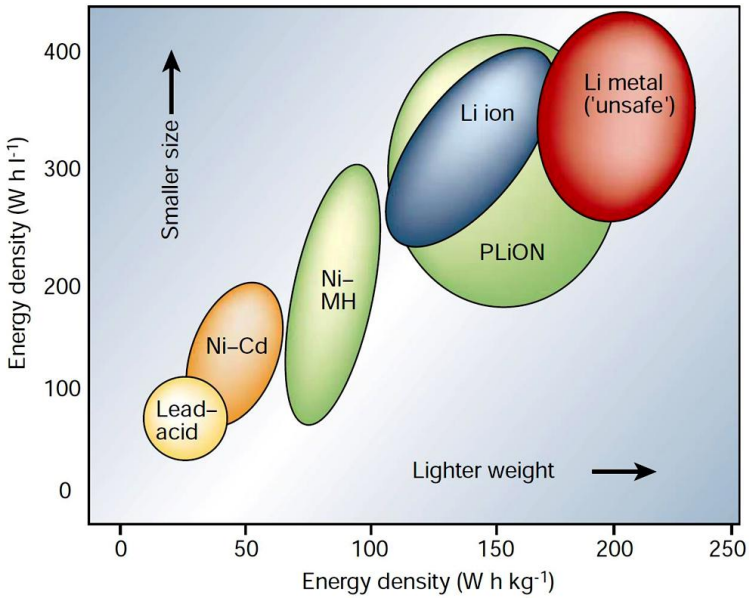

Figure 1: Comparison of the different battery technologies in terms of specific and volumetric energy density.[2]

The use of lithium-ion batteries in applications where long term reliability is required such as hybrid electrical vehicles (HEV), electrical vehicles (EV), stationary energy storage

systems for renewable energy sources and industry machines demands higher energy densities and increased lifetimes than what is currently available. New materials with high capacities for lithium storage are the key to meet the ever-increasing demand for energy density. Several conversion materials such as tin, sulphur and silicon, demonstrate a great potential for storing more lithium than the commercial intercalation material graphite. Unfortunately, their capacities often decrease rapidly after only a few cycles. This insufficient stability has become the major factor limiting their applicability. Lithium-ion batteries are complex systems and details of chemical reaction and side reactions of these novel materials in lithium cells are often not or only partly understood. The same is true for their degradation mechanisms. Various processes occur and interact during charge and discharge, which makes the independent investigation of individual processes particularly difficult.[3] Degradation processes can be of chemical but also of mechanical nature. Many chemical side reactions have been intensively researched in the last few years.[4-8] A significant amount of research has been spent on simulation of various mechanical effects in electrodes using different modelling tools.[9-13] However, only few experimental results of the mechanical behaviour of the electrode and its active material have been reported so far.[14,15] Further experimental research is needed to both prove and advance the simulation work and is helpful for understanding the interaction between the mechanical behaviour and chemical reactions in lithium-ion batteries.

This thesis focuses on the microscopic investigation of mechanical effects in intercalation materials and the local morphological changes that occur during electrical cycling of selected conversion materials. Two new methods for *in situ* and *ex situ* microscopic investigations will be introduced in Chapter 3. The main observations acquired using these methods on different electrode materials are then reported in Chapter 4. Besides detailed observations on conversion materials, these results include mechanical damage that occurs in $LiMn_{1.95}Al_{0.05}O_4$(LMAO) electrodes during cycling. The relationship of these effects to the underlying chemical reactions is discussed in Chapter 5 which also addresses the influence of cycle number and particle size on the mechanical damage. The damage that forms consists of cracks that partly form by brittle failure but also effects that can be described by mechanical fatigue were identified. The results of this thesis help to better understand local reaction in conversion materials and address the intercalation material LMAO which is of technological importance. For this material a detailed

picture of the mechanical response to electrical cycling emerged throughout this thesis. The results and interpretations presented in this thesis are of direct relevance for real batteries and may contribute to development of batteries with better long-term reliability in the future.

2 Background

Remarkable progress in lithium-ion battery technology promoted many new applications within the last few years. In this chapter, the theoretical background of the materials under investigation is reviewed. First, the working principle of lithium-ion batteries is introduced in section 2.1, and then the major properties and the degradation mechanisms of two typical intercalation materials for positive electrodes are presented in section 2.2 and 2.3. In section 2.4 the main chemical reaction and behaviour of two conversion materials for negative electrodes are introduced. Section 2.5 gives an overview of microscopic investigations of electrode materials that have been performed so far.

2.1 Working principle of a lithium-ion battery

Lithium-ion secondary cells have two electrodes with different chemical potentials. This potential difference determines the open circuit voltage (OCV) of the cell. A separator prevents the two electrodes from contacting each other. The electrolyte provides ionic conduction between the electrodes but isolates them electronically. When the electrodes are electronically connected by an external circuit, electrons flow from the negative electrode to the positive electrode in order to balance the potential difference. Meanwhile, positive lithium ions run in the same direction through the electrolyte. The stored chemical energy converts to electrical energy in the external circuit. In secondary lithium-ion cells this process is reversible meaning that they can be recharged by converting electrical energy to chemical energy. An external potential keeps the electrochemical reaction running in the opposite direction. Electrons flow from the positive electrode to the negative electrode with increasing potential difference, while lithium ions with opposite charge go through the electrolyte. In this process, the electrical energy is restored within the electrochemical cell (Figure 2). The reversibility of this charge and discharge process is of importance for the lifetime of a battery.

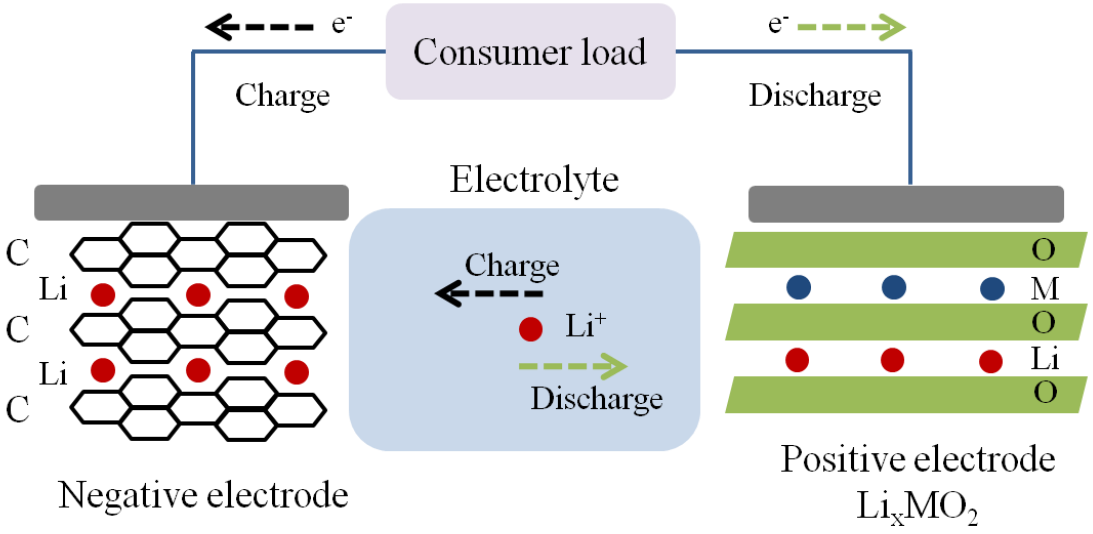

Figure 2: Schematic of the working principle of lithium-ion batteries.

The stored energy can be calculated by integrating the potential difference over the transported charge. The capacities of most battery systems decrease after several cycles. The corresponding cell voltage depends not only on the potential difference between the electrodes, but also on the kinetics of the reaction and impedance of the cell. Impedance increase leads to raised voltage plateaus during charge and lowered voltage plateaus during discharge, which causes power fading and the reduction of energy conversion efficiency. Hence the battery lifetime is often determined by both, capacity fading and impedance increase.

The mechanisms of capacity fading and impedance increase can be quite complicated. Most research focuses on side reactions between various components and impurities in the cells. The electrolyte could be oxidized by the delithiated positive electrode in high potential range and reduced by the lithiated negative electrode in low potential range. Impurities in the electrolyte can work as catalyst in these side reactions.[4-8] The kinetics of many side reactions depend strongly on cell voltage and temperature. For example at elevated temperature the degradation of many materials is accelerated. These side reactions cause a number of changes on electrode materials. The red-ox reaction between the electrolyte and the electrode leads to the formation of an interface layer, which results in capacity fading and impedance increase in different locations

in electrochemical cells. These effects occur often not separately. They could be influenced by different cycling behaviour, certain storage conditions or products of side reactions.

Side reactions are not the only reason for degradation. Lithium insertion/extraction also causes volume expansion/shrinkage. It is often the case that this process occurs inhomogenously. Consequently, stress is induced in the active material particles and even in the whole electrode.[9-13] In case of tensile stress, materials may crack.[9,16-22] These effects could disconnect the active material from the electronic conductive matrix and lead to loss of active material. More details of degradation mechanisms are described in section 2.3.

2.2 Intercalation materials for positive electrodes

Over the last two decades, intercalation materials have been commonly used as active materials for positive and negative electrodes in rechargeable lithium-ion batteries. These materials have relatively stable crystal lattice structures. Small lithium ions can be intercalated/de-intercalated in interstitial sites without significantly changing the main crystal structure. These systems are called "rocking chair" batteries,[1] where lithium ions rock between the two electrodes during charge and discharge. The cell voltage corresponds to given lithium content in the electrodes. The intercalation materials used in the lithium-ion batteries are chemically and mechanically quite stable. Many of them have relatively high potential versus lithium metal. However the specific capacities of the intercalation materials are limited to values below 200 mAh/g, which is a main problem for improving the specific energy density of such battery systems.

There are three main host structures which are used currently for lithium intercalation in the high potential range. Major properties of the standard materials with layered structure $LiCoO_2$ (LCO), with spinel structure $LiMn_2O_4$ (LMO) and with olivine structure $LiFePO_4$ (LFP) are shown in Table 1. Lattice structures of LFP, LCO and LMO enable either one-, or two-, or three-dimensional lithium diffusion, respectively. Among the intercalation materials of this thesis are materials of LCO and LMO type. In the following a brief description of both systems will be given.

Table 1: Major properties of the standard intercalation materials

Material	Potential vs. Li (V)	Theoretical specific capacity (mAh/g)	Reversible range Δx
layered $Li_{1-x}CoO_2$	3.9	137	0.5
spinel $Li_{1-x}Mn_2O_4$	4	148	1
olivine $Li_{1-x}FePO_4$	3.5	170	1

2.2.1 Layered structure

LCO is the standard active material which has been widely used for positive electrodes over the last decade for many mobile applications. LCO represents the layered-type structure that has a distorted rock-salt crystal with the symmetry of space group $R\bar{3}m$.[23-25] Lithium and the transition metal cobalt occupy alternatively the octahedral sites, namely on the (111) planes of a close-packed lattice of oxygen. The alternative (111) ordering of lithium and cobalt leads to a distortion of the cubic lattice to hexagonal symmetry. Oxygen and the transition metal cobalt constitute stable layered structures, in which the lithium ions could be stored (Figure 3). Many commercial positive electrode materials, e.g. $LiNiO_2$ (LNO), $LiMnO_2$, $LiMn_{1/3}Ni_{1/3}Co_{1/3}O_2$ (LMNCO) and $LiNi_{0.8}Co_{0.15}Al_{0.05}O_2$ (LNCAO) are members of this material group with layered rock-salt structure. LCO-lithium cells exhibit smooth charge/discharge plateaus around 3.9 V and operate between 3 V and 4.3 V, which corresponds to a variation of the lithium content in the range of $0 < x < 0.5$. [23-25]

$$LiCoO_2 \leftrightarrow Li_{1-x}CoO_2 + xLi^+ + xe^- \qquad (0 < x < 0.5)$$

The first order phase transition of two co-existing phases with space group $R\bar{3}m$ occurs in this range. Further lithium intercalation induces a distortion from hexagonal to monoclinic symmetry. This monoclinic phase can be detected around $x = 0.5$. The transformation to the monoclinic phase and the rearrangement in the stacking of the oxygen layer in the range of $x < 0.25$ leads to poor cyclability for charging the material to voltage higher than 4.3V.[26] This means that only half of the capacity can be reversibly used. The reversible phase transition of the lithium content range $0 < x < 0.5$ induces changes of the parameters of the hexagonal lattice. The delithiation leads to an increase of the layer distance of ~ 2% and a decrease of the Co-Co distances inside the Co layer.[27-29] The dimensional mismatch between the two phases induces stress near the phase boundaries.

Lithium ions can be transported within the layered structure and this material can therefore be characterized as a 2 dimensional conductor. The diffusion coefficient of lithium in LCO is measured and data fall into the range between 10^{-11} m^2/s and 10^{-12} m^2/s at room temperature. Lithium diffusivity in LCO is higher than that of many other materials for example

with spinel and olivine crystal structures. Besides the high mobility of lithium ions, LCO also exhibits excellent electronic conductivity. A transformation from semi conductivity to metallic conductivity was experimentally measured during the first order phase transition in the lithium content range $0 < x < 0.5$, which is a result of the overlap of the conduction bands of the solid phase.[30,31] Key advantages of LCO based materials compared to other materials are often the high electronic and lithium ionic conductivities.

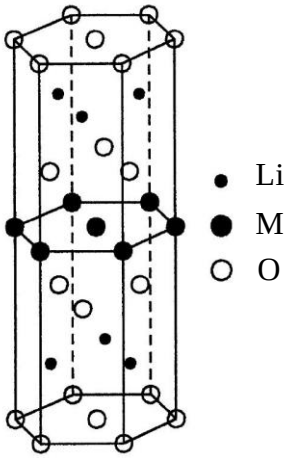

Figure 3: Schematic of layered structure of $LiMO_2$ with stacking of O-Li-O-M. [23]

2.2.2 Spinel structure

Mn is an abundant material and compared to LCO, manganese spinel LMO is inexpensive, non toxic, and is environmentally friendly. Additionally, the improved safety at the cell level is another major benefit for using manganese spinel as positive electrode material. The theoretical capacity and the electrochemical potential of LMO are similar to LCO. LMO reacts according to the following equation where several phase transformations occur within the full intercalation range.

$$LiMn_2O_4 \leftrightarrow Li_{1-x}Mn_2O_4 + xLi^+ + xe^- \qquad (0 < x < 1)$$

LMO spinel has a space group of Fd3m where oxygen forms a cubic close packed lattice on the 32e sites, lithium occupies 1/8 of the tetrahedral 8a sites and the transition metal Mn occupies 1/2 of the octahedral 16d sites. The empty tetrahedral 8a sites and the surrounding octahedral 16c sites build up a network, where lithium ions can move in three dimensions within the lattice.[32] The lithium diffusion coefficient in the spinel structure $Li_{1-x}Mn_2O_4$ ($0 < x < 1$) was found to lie between 10^{-12} m^2/s and 10^{-14} m^2/s at room temperature, which is significantly lower than that of LCO.[33-35]

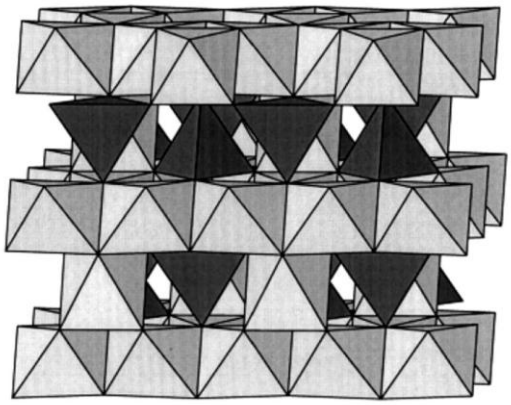

Figure 4: The three dimensional framework of the spinel $LiMn_2O_4$ lattice. [36]

The charge/discharge curve of a LMO-lithium cell has one S type plateau at ~4 V and one flat plateau around 4.15 V in the range of $0<x<1$. Within this voltage range several phases exist. Depending on the literature source, different phases were reported to form and coexist in the normal operating range between 3.5V and 4.5V. The actual phases that form and coexist during extraction and insertion of lithium seem to depend on the synthesis condition and doping elements in the material. In all cases, the lattice shrinks/expands when lithium is removed/inserted, which leads to a reversible volume change of the undoped material of ~ 2.3% during charge and discharge. The change in lattice constant is not a linear function of the lithium concentration and depends on the individual phases and phase transformations. [37-40]

2.3 Degradation of intercalation materials in positive electrode

Degradation of lithium-ion cells, such as capacity fading, power loss and impedance rise can be detected after battery operation under different conditions. Degradation processes in electrodes are of great technological importance and have been intensively studied. Major degradation effects have been attributed to some of the following mechanisms: [4-8]

- Binder decomposition
- Current collector corrosion
- Structural disorder of the active material
- Dissolution of electrode material in the electrolyte
- Mechanical damage of electrode materials
- Decomposition of the electrolyte
- Surface layer formation on the electrode materials
- Loss of contact between active material particles and electronic conductive matrix

All of these processes are either induced by chemical/physical reactions or combinations thereof and take place under different operation conditions and occur at various voltages. Of particular interest for this thesis are the subsets of physical reactions that are due to mechanical effects.

2.3.1 Degradation of spinel materials

The major degradation process of LMO as positive electrode material in lithium-ion cells is caused by the Jahn-Teller distortion in deeply discharged state and manganese dissolution in the electrolyte solvent. Deeply discharging of LMO to 3V versus lithium results in Mn^{3+} ion formation in the lattice, where lithium ions may migrate from tetrahedral 8a sites into the octahedral 16c sites. This results in an asymmetric unit cell distortion.[38] Due to Jahn-Teller effect,

the lattice symmetry changes from cubic to tetragonal.[32,41,42] This has severe consequences in the electrochemical behaviour in the 3V range where the reversibility of this material is rather poor. At these potentials, a disproportion of trivalent manganese (Mn^{3+}) into tetravalent Mn^{4+} and divalent Mn^{2+} takes place. The Mn^{2+} ions produced in the reaction dissolve in the electrolyte and are deposited onto the graphite negative electrode where they can enhance electrolyte decomposition. Consequences of the Jahn-Teller distortion are the degradation of both positive and negative electrodes.[43,44] Moreover, products of further side reactions, for instance MnF_2, $MnCO_3$ and oxides may build electronic isolating films on the active material particle surface. This process is a typical example that shows how complex and interlinked degradation processes can be and that several materials (both electrodes and electrolyte) can play together in the degradation of a lithium-ion battery.

Partial substitution of manganese in the 16d site with lower valent atoms (Li, Mg, Al, Ni(III), Fe(III), Co(III)) increases the average oxidation state of Mn ions above +3.5. In this way, the disproportion reaction and the Jahn-Teller distortion can be suppressed, which benefits the long-term stability of the electrodes and consequently the cycle life of the cell. For example Spinel $LiMn_{2-x}Al_xO_4$ compounds with partial substitution of Mn(16d) by Al(16d) exhibit strongly improved cyclability and rate capability at room and elevated temperatures compared to LMO. The two red-ox reactions at 4 V and 4.15 V indicate inactivity of Al substitution in the electrochemical process. The XRD diffraction suggests a cubic spinel structure with $Fd\bar{3}m$ symmetry for $LiMn_{2-x}Al_xO_4$ where the lattice parameter of $LiMn_{2-x}Al_xO_4$ decreases linearly with increasing Al substitution.[45] For x=0.05, $LiMn_{1.95}Al_{0.05}O_4$ has a lattice parameter that is 0.02 Å smaller than that of LMO. The variation in lattice parameter caused by lithium insertion and extraction becomes smaller with increasing Al content [46] which was explained by the stronger bond between Al-O in comparison to the Mn-O bond. A test cell with $LiMn_{2-x}Al_xO_4$ (x=0.3) exhibited a low capacity loss of 2% at 25℃ after 50 cycles, which was much smaller than the capacity loss of 14.2% observed under the same conditions for $LiMn_2O_4$.[46] Also small amounts of Al such as x=0.05 are beneficial for improving the reliability.

The spinel $LiMn_{1.5}Ni_{0.5}O_4$(LMNO) is formed by replacing 0.5 Mn in $LiMn_2O_4$ by Ni. This material shows a higher potential versus lithium than LMO. Lithium-LMNO cells exhibit

flat charge/discharge plateaus of ~ 4.7 V and have theoretical capacity of 147 mAh/g, which corresponds to a variation of the lithium content of $Li_{1-x}Mn_{1.5}Ni_{0.5}O_4$ in the range of $0 < x < 1$. The high potential makes LMNO a promising candidate for a future commercial positive electrode material with high specific power and energy density.

$$LiMn_{1.5}Ni_{0.5}O_4 \leftrightarrow Li_{1-x}\,Mn_{1.5}Ni_{0.5}O_4 + xLi^+ + xe^- \qquad (0 < x < 1)$$

2.3.2 Solid-liquid interface

Compared to the standard negative electrode material graphite, the specific capacities of the positive electrode materials are lower. This ultimately limits the energy density of the lithium-ion cells. Hence there is interest in searching for new positive electrode materials with higher voltage versus lithium and/or with higher capacities.

Besides synthesis of materials with higher voltages, the electrolyte and its electrochemical stability window is of importance for high energy batteries. The delithiated active materials of high voltage electrodes have a highly oxidative power in the charged state of a battery. If the lowest unoccupied electronic state of the positive electrode material lies below the highest occupied molecular orbital of the electrolyte, the electrons are transferred from the electrolyte to the electrode material. In this reaction, the electrolyte is oxidized by the positive electrode material and a passivating film can form on the surface of the electrode.[31] Depending on the details of this reaction, degradation of the electrolyte and the positive electrode material can cause an increase of the resistance at the interface leading to cell impedance increase or even capacity loss. A similar effect can happen at the negative electrode where the electrolyte can be reduced.

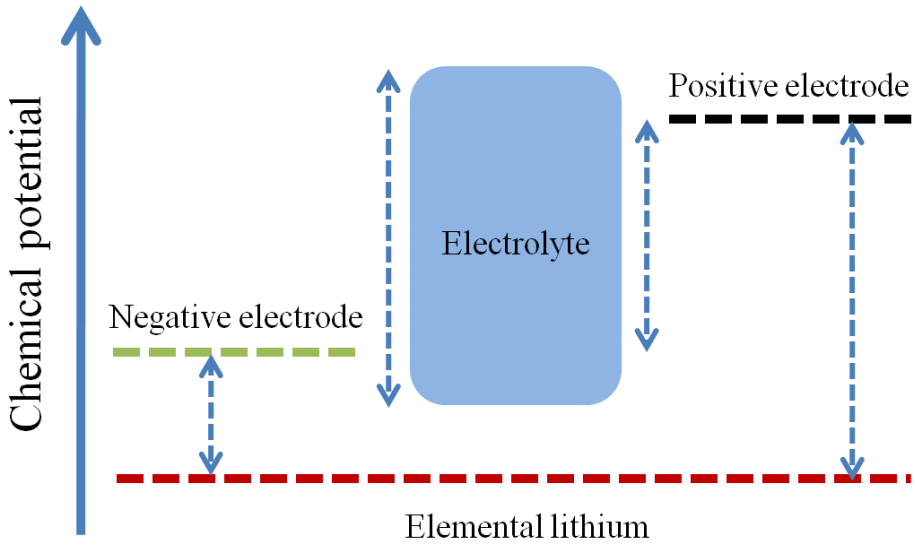

Figure 5: Electrochemical potential of the materials inside lithium-ion battery. The stability window of the electrolyte is marked in blue.

The red-ox reactions on the surface of the positive electrode material can be suppressed with several strategies. Some electrolyte additives are used to passivate the electrode surface.[47-49] Also new electrolytes with broader chemical stability window are intensively investigated to significantly reduce electrolyte oxidation. Another alternative is the surface modification of the high voltage positive electrode materials. Coating layers of inert materials onto the particle surface separates the oxidizing active material from the electrolyte to physically prevent the red-ox reactions. As a result, the inert coating layers improve the long-term cyclability of the cell.[50] Inert materials, such as Al_2O_3, $AlPO_4$ or RuO_2 can be used for surface coatings on the active material particles with layered structure and spinel structure, which decreases the capacity loss during cycling.[51-53]

Moreover, the use of electrically conductive materials for the surface coating can enhance the rate capability and lower the chemical potential at surface. This modification method is applied for LMNO by replacing 0.1 Ni with Fe. Compared to LMNO, LMNFO offers a better cyclability and higher rate capability. These excellent performances are results of the partial Fe-substitution. During the synthesis at high-temperature and the following cooling process, Fe ions segregate to the surface by themselves and form a Fe_2O_3 coating layer. This layer between solid

particles and the electrolyte could avert electrolyte decomposition and prevent formation of a thick isolating surface layer and therefore reduces the surface resistance. This morphology and its influence on the electrochemical performance have been proven experimentally.[54] The self-surface segregation offers a new alternative for improving the surface chemical stability with low processing cost. A high lithium ion diffusion coefficient in the order of 10^{-9} m^2/s was measured in the LMNFO bulk. This high diffusion coefficient might be due to stabilization of the disordered structure which improves the lithium intercalation and stronger Fe-O bonding which weakens the Li-O bonding, thereby easing lithium ion insertion in the host lattice.[55]

Most of the positive electrode compounds have low intrinsic ionic lithium conductivities and electronic conductivities, which can limit the reaction kinetics of the whole cells. Synthesis of small particles with dimensions on the nanometer scale is a common strategy to overcome this material problem. A high surface area/volume ratio reduces the diffusion/conduction length and increases the interface area between the active material and the electrolyte which together leads to an increase in the rate capability. However, more solid/electrolyte interface area do not only improves the lithium intercalation but also affects the side red-ox reactions, the solid-electrolyte-interface (SEI) formation and therefore can lead to irreversible capacity loss. A linear dependence of the electrolyte oxidation on the particle surface area has been experimentally measured.[56] Moreover, nano-structured electrodes with high surface areas may also induce some safety problems due to their enhanced reactivity. The particle size is therefore not only determining the electrochemical performance but also affecting safety and aging of a battery. It is therefore often necessary to compromise between these aspects and synthesize particles of optimum size for a given application. As will be shown in Chapters 4 and 5, there is also a strong effect of particle size on mechanical degradation and the long term reliability of certain electrode materials.

2.3.3 Mechanical effects in intercalation materials

All intercalation materials mentioned above exhibit lattice constant changes by lithium ion insertion and extraction due to valence change of the transition metals.[36] The change in the

lattice parameter is not necessarily a homogenous process. During the electrochemical reaction, lithium ions are first inserted in the particle surface and, then they diffuse into the bulk material. This leads to a lithium concentration gradient inside the particles. As a result, the related lattice misfit induces stresses in the particles.

Recently, intercalation induced stresses in the particles and their impact on the battery life-time has attracted much interest. Different mathematical models have been developed to understand the evolution of lithium concentration and the related stresses, which may cause fracture of the active materials. Cheng and Verbrugge have developed analytic solutions for the stresses distribution and their evolution within a spherical element during lithium de-/intercalation in single phase.[9,10] A dimensionless electrochemical Biot number in heat-transfer problems was used to describe the reaction kinetics and the diffusion conditions at the particle surface and inside the particles, which corresponds to the interfacial resistance and the diffusion resistance. Large Biot numbers represent small interfacial resistance and large lithium gradient in the solid. They found that tensile stresses and shear stresses were induced in the particles during both charge and discharge. The maximum tensile stresses are induced in the centre of particles in both radial and tangential directions during lithium intercalation. During lithium extraction, the maximum tensile stresses are formed at the particle surface in the tangential direction. The dimensionless electrochemical Biot number strongly affects the lithium concentration distribution and thereby the intercalation induced stresses (Figure 6), which means that the interfacial kinetics and the ionic diffusion in the particles play a critical role in the mechanical behaviour of the electrode.

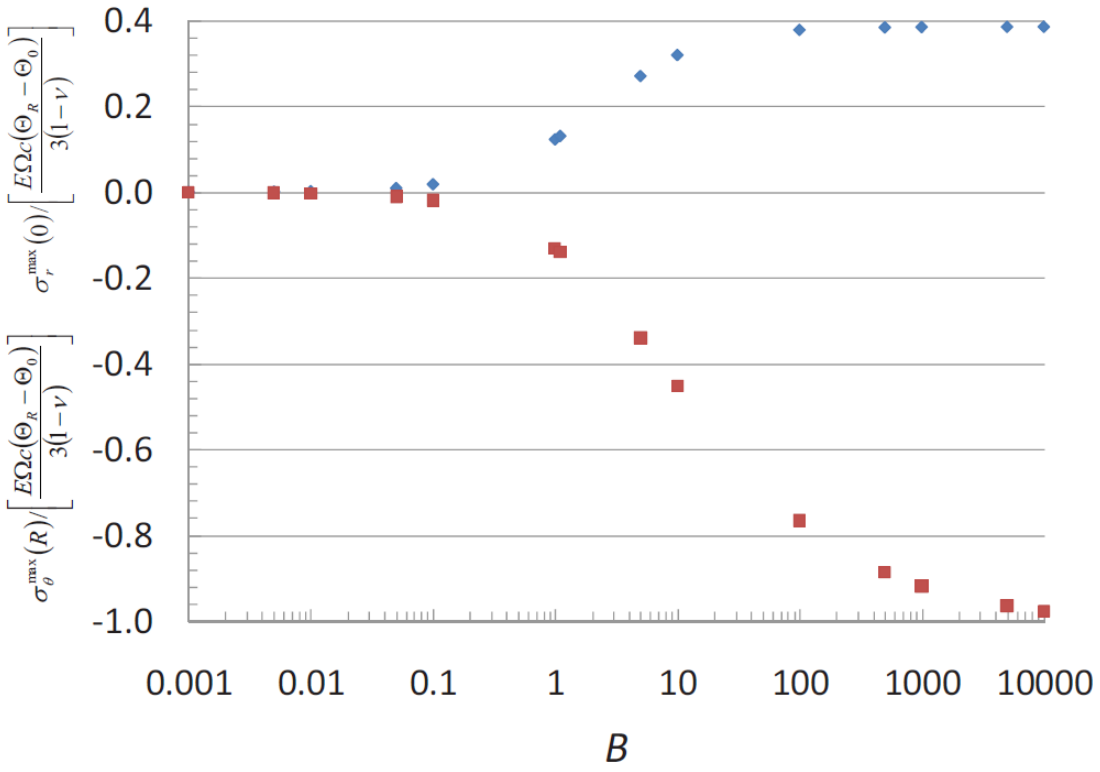

Figure 6: Maximum radial (tensile (+), in blue) and tangential (compressive (-), in red) stresses in the particles within a range of the electrochemical Biot number values during lithium insertion. The stresses $\sigma_r(R)$ and $\sigma_\theta(0)$ are nondimensionalized through dividing by $E\Omega c(\Theta_R-\Theta_0)/3/(1-\nu)$, where E is Young's modulus, Ω is the partial molar volume of the solute, c is the concentration of sites available for lithium insertion, Θ is the concentration of the filled host site, and ν is Poisson's ratio. For more details of the analytic solutions see [9].

Another source of stresses is independent of the insertion and extraction kinetics. Besides changes in lattice parameters, lithium insertion/extraction into/out of host materials often causes phase transformations. Here stresses are due to the coexistence of two phases and appear when two phases with different lattice parameters or crystal symmetries are in contact. This is a phenomenon common to most materials and happens in many layered structures, spinels, and olivines. Deshpande et al. analytically described the stresses evolution at the phase boundaries during the phase transformation and its dependence to the material parameters.[11] They used a core-shell structure to simulate the moving interface between a lithium rich phase and a lithium

poor phase during lithium extraction (Figure 7, Figure 8). In their model the lithium rich core is under compressive stress due to the shrinkage of the shell. In the lithium poor phase, the calculated stress is compressive in the radial direction and tensile in the tangential direction (Figure 9). The maximum tensile stress is found at the particle surface. At the phase boundary, a stress discontinuity is found in the tangential direction, where the compressive stress in the lithium rich phase changes to tensile stress in the lithium poor phase (Figure 10). This stress discontinuity depends strongly on the ratio of Young's modulus and the volume ratio of the two coexisting phases.

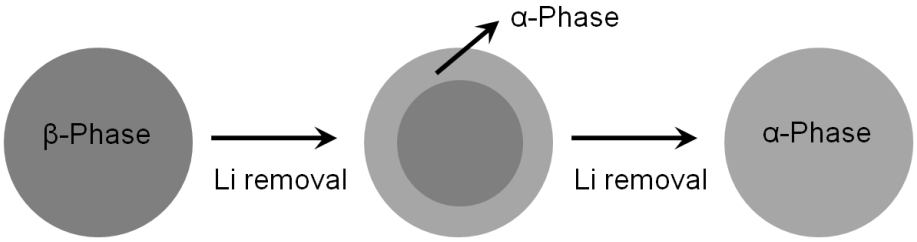

Figure 7: Core-shell model simulating a moving interface between a lithium rich phase β and a lithium poor phase α during lithium extraction.[11]

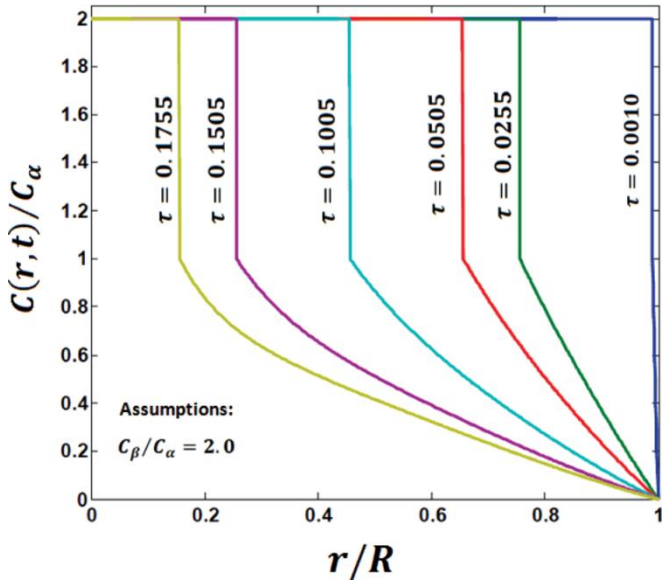

Figure 8: Concentration profile during phase transformation induced by lithium extraction.[11]

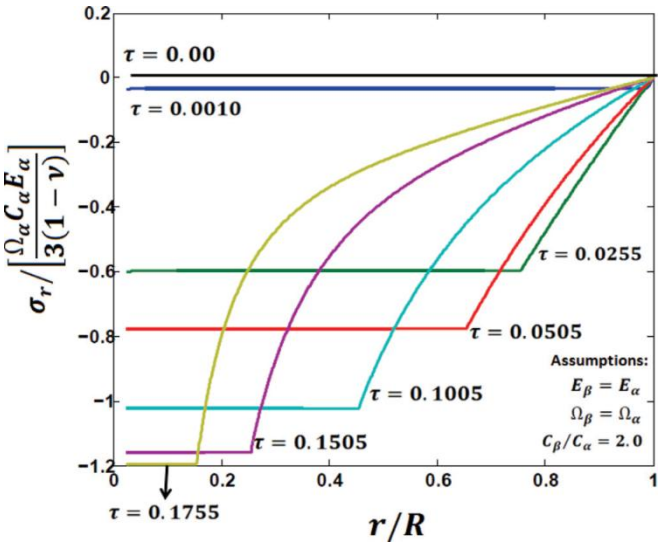

Figure 9: Stresses components along the radial direction induced by a phase transformation happening during lithium extraction. The radial stress σ_r is nondimensionalized through dividing by $\Omega_\alpha C_\alpha E_\alpha/3/(1-\nu)$, where Ω is the partical molar volume of the solute, C is the molar concentration, E is Young's modulus and ν is Poisson's ratio.[11]

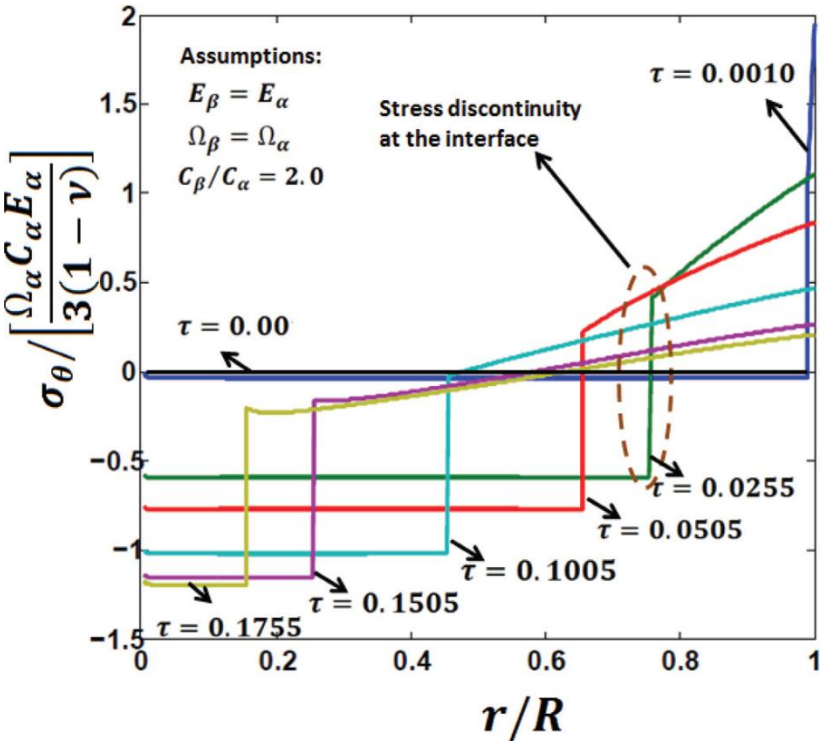

Figure 10: Stresses components along the tangential direction induced by a phase transformation happening during lithium extraction. The tangential stress σ_θ is nondimensionalized through diving by $\Omega_\alpha C_\alpha E_\alpha/3/(1-\nu)$, where Ω is the partical molar volume of the solute, C is the molar concentration, E is Young's modulus and ν is Poisson's ratio.[11]

Intercalation and phase transformation induced stresses may directly induce fracture of electrode particles and lead to capacity fading and impedance increases.[5] Various models which suggest criteria for crack initiation and growth to predict fracture have been proposed in the literature.[9,16-20] In some reports, a dependence of fracture on the particle size and current density has been established.[21,22] Zhao et al. developed a model where small particles and slow charge/discharge rate reduce the risk of fracture.[21] In this model there is a critical size below which crack formation can be avoided for a given charge/discharge rate.[21] A similar result can be seen in the model by Woodford et al., who developed an "electrochemical shock map" which predicts a critical charge rate as a failure criterion for individual electrode particles. This critical rate increases with decreasing particle size and increasing fracture toughness (K_C).[22]

2.4 SnO_2 and $CuCr_2Se_4$ as conversion materials

Compared to intercalation materials, many conversion materials have considerably larger theoretical capacities for storing lithium. In conversion materials, chemical reactions with lithium happen locally and in comparison to intercalation materials, drastic changes in chemistry, morphology and structure occur. One example of a conversion reaction is the reduction of an oxide and the formation of a metal. In this reaction the active material M_bX can be reduced to form Li_aX and metal M. In some cases these reactions show some reversibility (Reaction 1). In some cases the metal M can further alloy/de-alloy with lithium (Reaction 2).[57,58]

$$M_bX + aLi \leftrightarrow Li_aX + bM \qquad \text{(Reaction 1)}$$

$$M + cLi \leftrightarrow Li_cM \qquad \text{(Reaction 2)}$$

The oxidation state of M in the M_bX compound determines the specific capacity for the storage of lithium. Compared to the metallic elements in the intercalation materials, many metallic elements in the conversion material can be reduced or oxidized further during lithium insertion and extraction. Hence the theoretical capacities of these compounds are also larger.[57]

Despite their high capacities, there are several problems associated with such conversion materials. When the material is used as negative electrode, due to metallic alloying, the electrochemical potential of the alloy increases compared to pure lithium, which results in a reduction of the cell voltage. Lithium insertion/extraction into/from many conversion materials causes large volume expansions/shrinkages, which are larger than that of intercalation materials. These volume changes may induce large stresses and can destroy the electrode structure. As a result, the conductivity of the electrode decreases and the internal resistance increases. Furthermore, new phases are formed during the reaction with lithium. In the case where the new phases are no longer in contact with the matrix, the reaction can become irreversible. For these reasons, many conversion materials only show a small fraction of their theoretical capacity in real cells. The measured capacities of many conversion materials are known to decrease rapidly after only a couple of cycles.

The conversion materials tin oxide (SnO_2) and chromium copper selenide ($CuCr_2Se_4$) are investigated in this work. Both are materials can be used for negative electrodes. $CuCr_2Se_4$(CCS) is an interesting model system which shows a novel reaction mechanism. It has a spinel-type crystal structure (space group $Fd\bar{3}m$). In this structure, selenium atoms build up a cubic close packed lattice, in which the copper and chromium atoms are coordinated in the tetrahedral and octahedral sites. CCS shows metallic electronic conductivity. The ionic configuration is approximately $Cu^{+}Cr_2^{3.5+}Se_4^{2-}$.[59] Bodenez et al. found a combined displacement and intercalation mechanism in this spinel type during an electrochemical reaction with lithium.[60,61] Details of the reaction pathway and the reversibility are not known yet. Lithium insertion reaction in this spinel system is interesting because of the effects of anion and cation substitution on the reaction mechanisms.[62]

Tin (Sn) reacts with lithium and forms a Li_xSn alloy ($0 \leq x \leq 4.4$) at room temperature (Reaction 4, Figure 11). This reaction is reversible and Sn can be used as an electrode material for reversible lithium storage. Li_xSn alloy has a relatively low voltage versus pure lithium and shows a large theoretical capacity of 991 mAh/g (Figure 13).[63] This capacity is almost three times that of graphite which is today's standard negative electrode material. Unfortunately, Sn shows a rather poor reliability as electrode material. This may be due to the 3.6 fold volume expansion that occurs during lithium insertion.[64] Such large volume expansions may induce mechanical stresses and crack initiation in the electrode. Consequently, the conductivity of the electrode is reduced, the capacity decreases and the internal resistance increases, resulting in a poor cycling stability (Figure 13).[63]

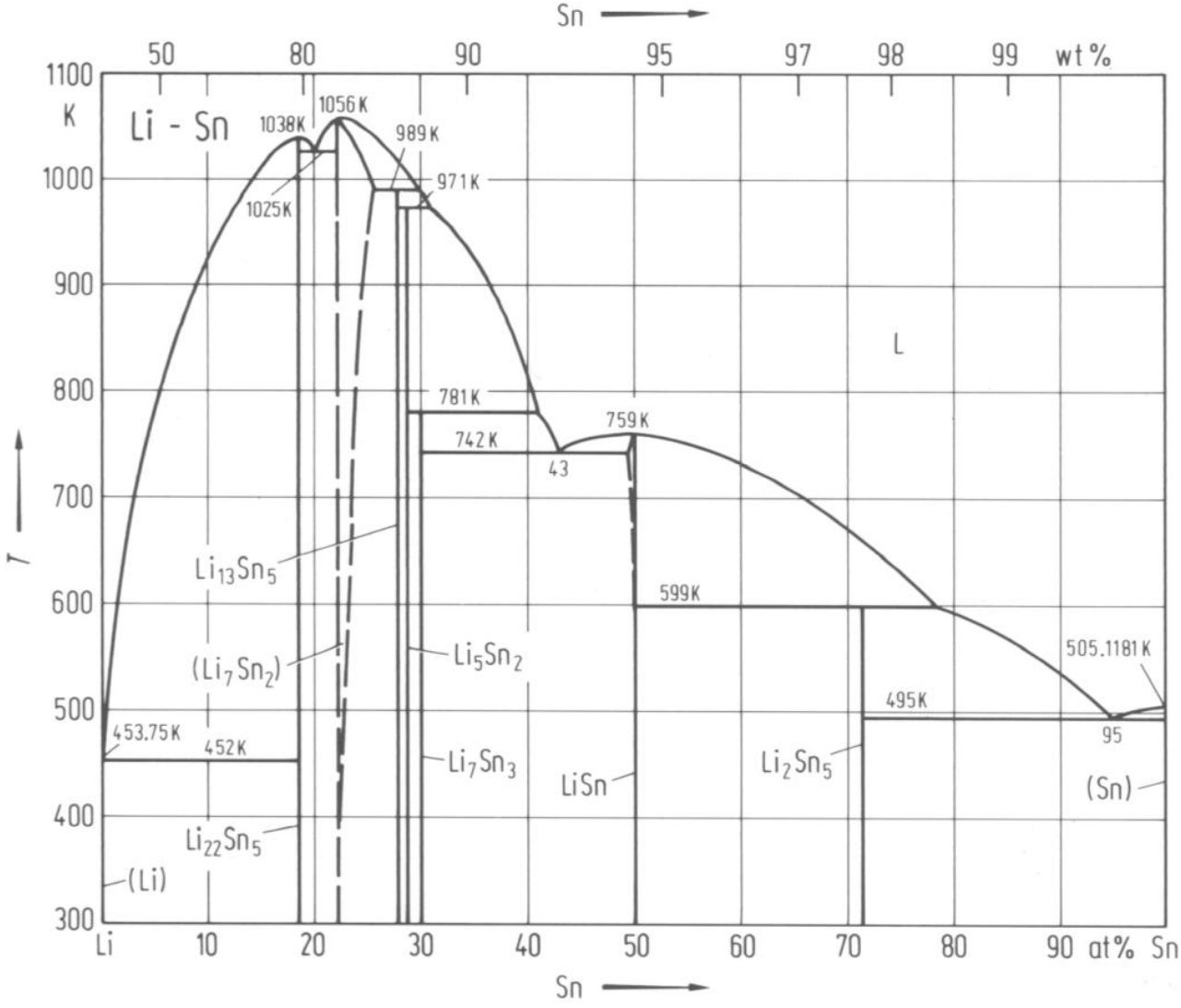

Figure 11: Phase diagram of Li-Sn.

$4\text{Li} + \text{SnO}_2 \rightarrow 2\text{Li}_2\text{O} + \text{Sn}$ (Reaction 3)

$x\text{Li} + \text{Sn} \leftrightarrow \text{Li}_x\text{Sn}\ (0 \leq x \leq 4.4)$ (Reaction 4)

One concept to increase the cycle life of tin-based electrodes is to use SnO_2 as the starting material. In an initial reaction the oxygen from the SnO_2 reacts with lithium to form an amorphous Li_2O matrix and elementary Sn (Reaction 3). It is speculated that the reduced Sn is dispersed in the form of very small particles inside the Li_2O matrix. This matrix may help to distribute stresses that occur in the Sn particles during alloying with lithium. The Li_2O matrix

improves the cycling stability of the electrode by preventing the Sn metal particles from agglomerating. Once significantly large Sn entities are formed, the large volume changes induce sufficient stresses to damage the matrix (Figure 12).[63] The theoretical capacity of SnO_2 of the first discharge based on formation of Li_2O and lithium alloying with Sn is 1491 mAh/g.[63] The theoretical capacity of the second discharge based on $Li_{4.4}Sn$ alloying is 781 mAh/g. The capacity of the second discharge is assumed to be reversible. The observed capacity is commonly smaller than the theoretical value and decreases during electrical cycling (Figure 13).

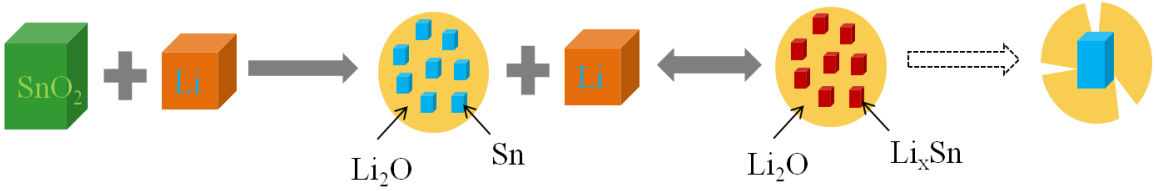

Figure 12: Mechanism for lithium storage in SnO_2 particles.

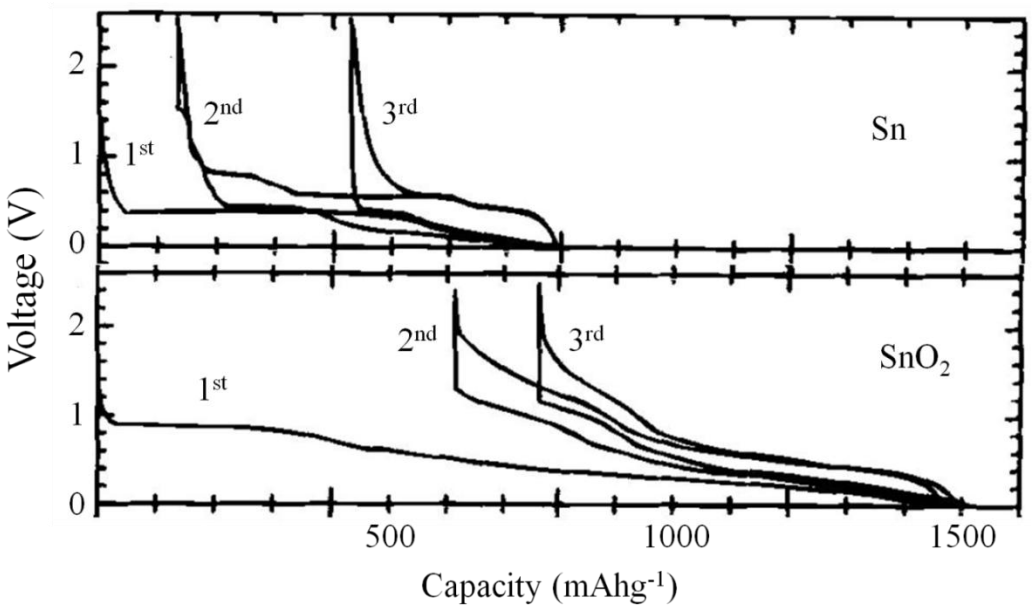

Figure 13: Voltage profile of Sn and SnO_2 versus lithium in the first three cycles.[63]

2.5 Microscopic investigations of electrodes

Typically new battery materials are tested using galvanostatic charge/discharge or cyclic voltammetry which can only give spatial averages of the battery behavior and does not account for the local aspects that occur inside a battery. Also other testing methods commonly employed such as electrochemical impedance spectroscopy (EIS) or *in situ* X-ray diffraction (XRD) can only be used to monitor spatial averages of an electrode. Since electrode materials are inherently nano-scale materials, local observations of these materials at high resolutions can be helpful to understand the microscopic processes that occur inside nano-particles and at their interfaces with the electrolyte. *In situ* optical microscopy of the electrode materials has been carried out by several research groups.[65-67] However, the resolution of optical microscopy is rather limited and is often too low for most of the nano-scale materials.

Scanning electron microscopy (SEM) and transmission electron microscopy (TEM) offers a much higher resolution but is difficult to perform on a working battery due to the high level vacuum that is needed and the presence of high energy electrons which can interfere with the battery operation. In previous SEM investigations of lithium batteries,[68,69] the cells had to be dismantled and the electrolyte had to be removed before they were observed. Risk of damage and contamination are significant in this case and extreme care needs to be taken to keep the battery materials away from atmosphere or moisture where they could be altered by the reactions with oxygen, nitrogen or water.[70]

Previous attempts of *in situ* SEM battery experiments have been pursued by several groups.[71-73] The different concepts for SEM observations are briefly summarized as follows: Baudry et al. [71] used a polymeric electrolyte. Because of the low ionic conductivity, the batteries had to be heated to achieve reasonable rates. The influence of the heating on the battery could not be investigated. During the transfer process to the vacuum chamber of the SEM, the battery was in contact with the atmosphere for about 30 seconds. Orsini et al. [72] used an electrolyte that is commonly used in commercial batteries consisting of ethylene carbonate/dimethyl carbonate solution with 1 M $LiPF_6$ salt. After a given number of cycles the batteries were cooled to -20 ℃ to freeze the electrolyte and then transferred into the SEM under protective atmosphere.

Contamination could be prevented in this way but the batteries could not be electrically cycled inside the SEM. Another approach was taken by Raimann et al. [73], who used carbonate solvents (ethylene carbonate and propylene carbonate) with high boiling point as an electrolyte in an *in situ* environmental scanning electron microscope (ESEM). ESEMs allow the imaging of samples with higher vapor pressures. In certain cases even wet samples can be imaged. Unfortunately, the resolution of such SEMs is typically reduced due to scattering of electrons in the gas atmosphere that is present inside the SEM chamber. Since the electrolyte evaporated, experiments had to be carried out quickly. Recently, Huang et al. [74] constructed a electrochemical cell inside a high-resolution transmission electron microscope (HRTEM), consisting of SnO_2 nanowires as the anode, an ionic liquid based electrolyte, and LCO as the cathode material. By using this setup, they successfully observed the lithiation process of the SnO_2 nanowires *in situ*. The experiment was controlled by a potentiostat during electrochemical charging and important details of material evolution that comprise the lifetime of the cell was found.[74]

In this work an alternative attempt was used. *In situ* SEM experiments were performed in high vacuum using an ionic liquid based electrolyte. This experimental concept combines high resolution imaging with real-time observation during galvanostatic charging and discharging of the electrochemical test cell. Experimental details can found in section 3.3 and results from this method are presented in section 4.1.

2.6 Aims of this work

Although many calculations and simulations of stress distributions [9-13] and mechanical failure processes [21,22] in electrodes for lithium batteries have been performed, so far there are only a limited number of experimental observations of the mechanical behaviour of electrode materials in batteries.[14,15] Experiments focusing on the detailed microscopic and mechanical response of electrode materials are useful to assess the importance of mechanical effects for the cycle life of real batteries. This work focuses on the microscopic and mechanical behaviour of different electrodes for lithium-ion batteries. SEM observations were used to investigate electrode materials. In order to perform these experiments experimental techniques have been developed and applied to a set of materials.

Battery experiments on electrodes made from conversion materials SnO_2 and CCS have been performed *in situ* inside the SEM. Aims of these experiments are the exploration of reaction pathways and to investigate reversibility and associated processes during battery operation. Of interest were the observations of effects on the particle surfaces and the observation of volume expansions and associated morphological changes and how these effects influence the reversibility of the electrochemical reactions in the cell.

Besides conversion materials, electrodes containing commercial intercalation materials LMAO, LCO and LNMFO have been tested in electrochemical cells and investigated *ex situ* by SEM. In these experiments it was possible to test electrodes up to several hundreds of cycles and interrupt cell operation at any time to monitor changes in the electrodes. This work concentrated on the mechanical processes occurring in real batteries. The results show that mechanical effects and damage are prevalent even in conventional batteries. The acquired lifetime data and the detailed observations and descriptions of the mechanisms help to obtain a clearer picture of the mechanisms governing battery operation and may be used in the future to prove and advance simulation efforts.

3 Experiment

The chemical reactions and physical processes occurring inside lithium-cells determine both battery performance and life time. Common batteries and electrochemical processes are characterized by various experimental methods such as electrical measurements, diffraction or spectroscopy techniques like XRD, NMR or EIS and other volume averaging techniques as mentioned in the last chapter. Besides these tools that average over relative large volumes, local investigations are useful to identify and explore mechanisms in batteries. Local investigations with high spatial resolution are motivated by two reasons. First, the use of powders with small particle sizes which are often only a few tens of nanometers has become a common strategy for using new materials and enhancing the performance of batteries. Second, many reactions occur inhomogenously in the electrodes and a high spatial resolution is needed. For these reasons, in this thesis methods have been developed that allow for the investigation of electrode materials in high resolution inside an SEM. Section 3.3 introduces a special *in situ* technique and section 3.4 describes a technique that has been developed to enable investigation of electrodes after a large number of cycles. This method is also non-destructive and the same region of an electrode can be compared after different numbers of cycles.

3.1 Electrical measurements

Electrical measurements help to characterize reactions occurring in electrochemical lithium cells. In lithium-ion batteries, one electron moving in the external cuicirt always corresponds to a lithium positive ion running through the electrolyte. Therefore, the lithium content in the active material measures the state of charge (SOC) of a secondary lithium ion cell. SOC can not be directly determined and is typically identified by measuring OCV or transferred electrical charge Q.

OCV corresponds to the chemical potential difference between the two electrodes and can be usually estiamted from the cell voltage V by using a correction term that depends on the cell impedance, the used current and the cell temperature. Due to small voltage changes in the

charge/discharge plateaus and complicated measurements, this methode is difficult to apply for lithium-ion batteries.

Alternatively, SOC can be calculated by integrating current in time. A cell voltage is defined as SOC = 0. Changes of SOC can be then easily estimated by the transferred electrical charge. This methode is used in this work for calculating SOC, lithium content in the active materials, and active cell capacity. Furthermore, the relationship of OCV and cell voltage during charge and discharge can be used to determine the cell resistance changes. In this work, the capacity and resistance changes are values used to characterize the cell degradation, which is caused by the micro-structural evolution of electrode materials upon lithium insertion/extraction.

Electrochemical cells are commonly tested in two basic modes, either under current or voltage control. The current-controlled galvanostatic mode is often used for measuring long term behaviour of a cell, while the potential controlled voltammetry mode is more suitable for measuring reaction kinetics. For determining the degradation behaviour in long term cycling, a potentiostat/galvanostat (VMP3, Bio-logic SAS, Claix, France) with the current controlled mode "galvanostatic cycling with potential limitation (GCPL)" was used for all *ex situ* Swagelok-cells in this work. The lithium cells for *in situ* SEM observation were also cycled galvanostatically with potential limitation using a Keithley 2400 series source-meter controlled by a home-built Labview^{TM} program.

During the galvanostatic tests, the cells were cycled by applying a constant charge/discharge rate. The charge/discharge rates are commonly expressed as C/h, where h is the time needed, in hours, for charging/discharging the battery with the nominal charge. Typical rates in the experiments ranged from C/20 to 5C. During the tests, cells were always cycled within a given voltage range for preventing cells from overcharge or deep-discharge. Due to the potential limitation of the galvanostats, the current was always reversed when one of the voltage limits was reached, so that the cell was cycled within the voltage window. By using a constant charge/discharge current, the transferred electrical charge can be easily calculated by multiplying current by time. In other words, the measured charge changes linearly with the test time.

Incremental capacity analysis

During galvanostatic charge and discharge, the electrochemical reactions take place at a constant rate. The rate of voltage change is extremely low during charge/discharge plateaus. In other words, the incremental capacity (IC) is relatively high at these voltages. IC Peaks can be found in a diagram, where dQ/dV (Q: transferred electrical charge, V: cell voltage) is plotted versus the cell voltage. Such a diagram bears resemblance to cyclic voltammetry and can be used for quantifying the electrochemical process in the cells.[75]

Due to ageing effects, the measured parameters such as the IC peak value and the related voltage often change with the number of cycles. Typical changes are shown in Figure 14 and Figure 15 by comparing the curve in solid (begin of life) and the curve in dash (end of life). When the IC decreases, the cell loses charge/discharge capacity, which can be recognized in Figure 14 by comparing the curves. Figure 15 shows a peak shift to higher voltage values during charge and to lower voltage values during discharge, while the shape of the peak keeps unchanged. This observation indicates increasing ohmic resistance of the cell. The measured IC curve in the practice normally contains a combination of different mechanisms. Incremental capacity analysis (ICA) allows a continuous detecting of the cell degradation in the form of resistance increase or capacity loss. However, the absolute value of impedance cannot be measured in a galvanostatic test.

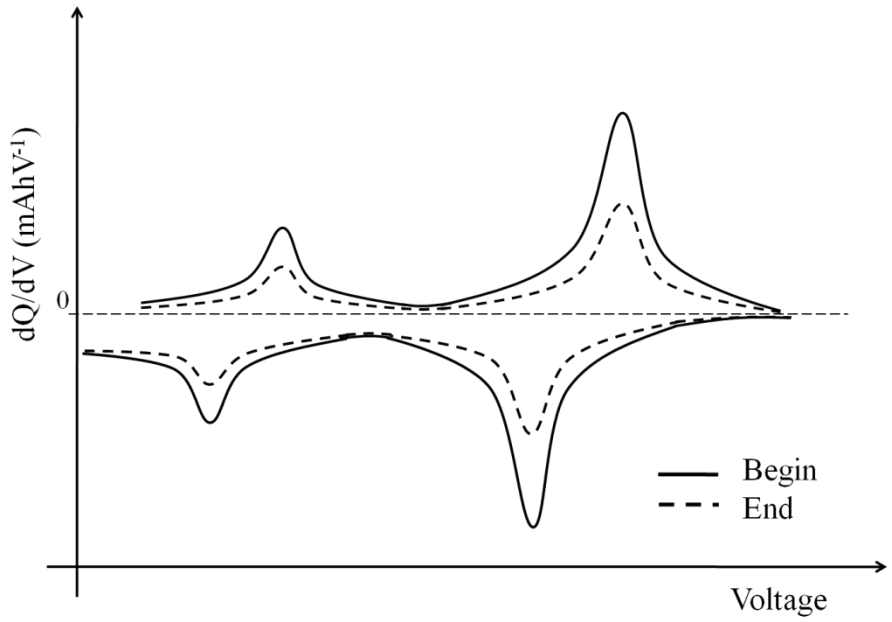

Figure 14: Decreasing IC value indicates capacity fading by comparing the curves of begin of life and end of life.

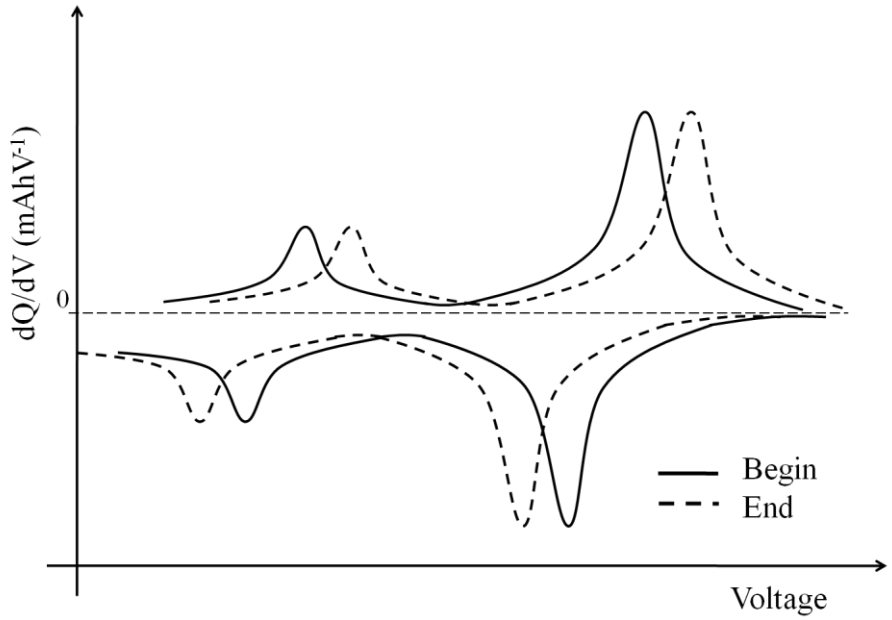

Figure 15: Voltage shift suggests ohmic resistance change by comparing the curves of begin of life and end of life.

3.2 Sample preparation and electron microscopy

Before the details about the electron microscopic methods are introduced, a brief description of the microscope will be given. For all of the experiments, a dual beam SEM/FIB (FEI Nova Nanolab 200) was used. It was used for imaging and in a few cases for cross sectioning active material particles in the working electrodes by using the ion beam. In this microscope, an electron column is placed above the sample stage which emits an electron beam for sample imaging at high resolutions down to ~ 1 nm. The gallium-ion source is mounted at an angle of 52 ° relative to the electron column (Figure 16). The gallium-ion beam generated from the ion source can be used for both imaging and machining particles with a maximum resolution of ~ 7 nm. The sample can be simultaneously imaged by the electron beam and machined by ion beam at the eucentric height, where the two beams intersect on the sample surface. Besides rotation, the stage can be tilted from -10 ° to +52 °, so that the particles can be machined and imaged at different angles.

The SEM images of the working electrodes, which were electrically cycled in the Swagelok-cells, were taken at 10 kV acceleration voltage at a beam current of 0.54 nA. Some particles were machined by gallium-ion beams with 30 keV energy. The cross sections of these particles were then imaged using the electron beam.

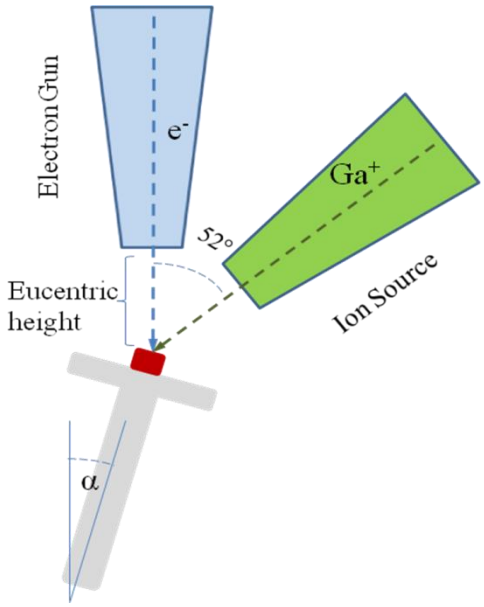

Figure 16: Schematic of dual beam microscopy system SEM/FIB.

3.3 *In situ* SEM experiments

The *in situ* lithium cell consisted of two electrodes and was designed in a way that allows for the observation inside the SEM. Therefore it had to be vacuum compatible and needed to be electrically connected through the microscope. The lower electrode consisted of pure lithium (99.9% purity, 0.12 mm thick, Goodfellow). The working electrode, which contained the material under investigation, was placed on the top of the cell stack (Figure 17).

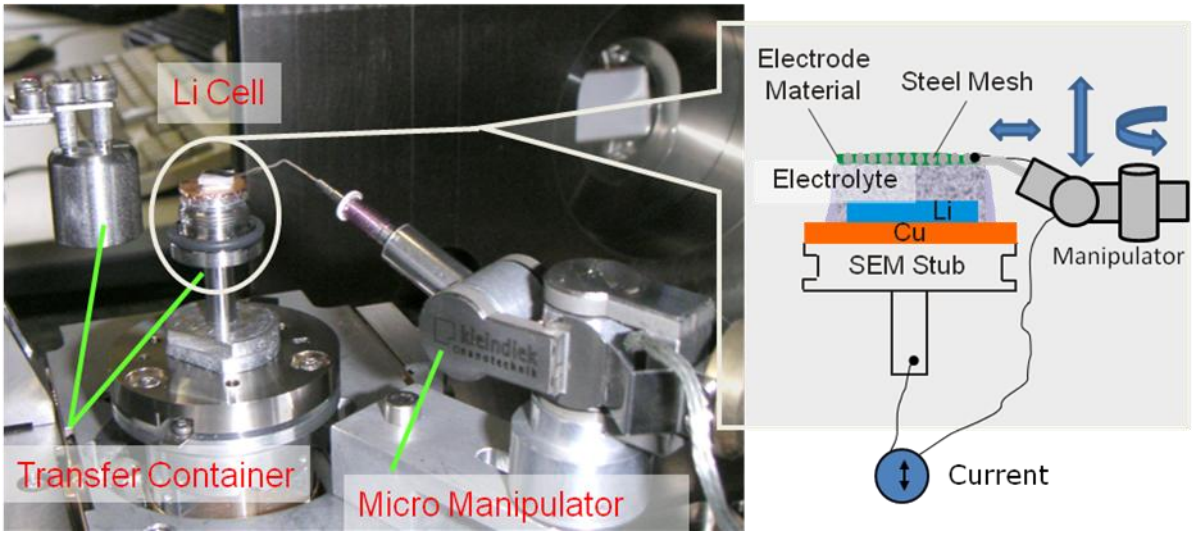

Figure 17: Setup of the lithium cell for the *in situ* SEM observation.

The working electrode had to be permeable for the electrolyte and therefore a stainless steel mesh (DIN 1.4401/AISI 316) was used as current collector. As in normal batteries, the electrode coating on this mesh was composed of the active material, polyvinylidene fluoride (PVDF) as a binder and carbon black for enhancing electronic conductivity. These materials were milled and mixed using mortar and pestle, and then several drops of N-methyl-2-pyrrolidone (NMP) were added to dissolve the PVDF binder. The slurry was then coated onto the stainless steel mesh and dried in air at room temperature for 24 hours. Additional drying occurred in a furnace at 90 ℃ for another 24 hours in order to remove the remaining NMP and

minimize water content. For the electrolyte, an 0.5 M solution of lithium-bis(trifluoromethanesulfonyl)imide (Li-TFSI lithium conductive salt) in buthylmethylpyrrolidinium-TFSI (BMPyrr-TFSI, ionic liquid, provided by Ionic Liquid Technologies GmbH, Heilbronn, Germany) was used. The water content of the ionic liquid (IL) was investigated using coulometric Karl-Fischer titration and values below 120 ppm in the as received state and below 30 ppm in the additionally dried state were determined. Due to its very low vapour pressure, the ionic liquid solvent could be easily used inside the vacuum of the SEM chamber. Preliminary tests showed that this electrolyte was even compatible with ultra high vacuum (pressures below 10^{-8} mbar). As a separator, a laboratory filter paper (100% borosilicate glass microfibre GF/B from Whatman) was used.

Several steps were needed to assemble the test cell. First, the lower part was assembled inside a glove box under protective argon atmosphere and the upper part containing the working electrode was placed on top of separator inside the SEM. Next, for the lower part, a standard SEM stub made from aluminium was covered by a thin copper foil (99.9% purity, Goodfellow). After that, a small piece of lithium was mounted onto this copper foil and the separator was placed on top of it and soaked with a few drops of the IL-based electrolyte. Once completed, the lower part of the cell was ready for transfer to the SEM. Since it contained the electrolyte and elementary lithium, it had to be protected from the atmosphere during transfer. For this purpose, a home-built transfer system was used. It consisted of a small container that hermetically enclosed the lower part of the test cell and was mounted into the SEM chamber (Figure 18). After the chamber of the SEM was pumped to ~10^{-5} mbar, the container was opened. The transfer system could be opened and closed using the motion and rotation of the SEM stage.

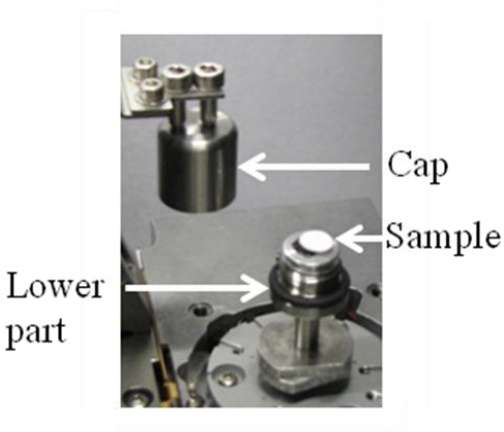

Figure 18: Setup of the transfer container used inside the SEM chamber.

For further assembly of the battery inside the SEM, the working electrode had to be placed on top of the separator. This was done using a micromanipulator (Kleindiek MM3A-EM, Kleindiek GmbH, Reutlingen, Germany). Prior to closing the chamber, a steel mesh was clamped to the manipulator and therefore the manipulator also provided the electrical contact to the working electrode. The other electrical contact to the counter electrode was established through the SEM chamber and the conventional electrical grounding of the SEM (Figure 17).

Assembling the cell in this two stage process proved to be very useful because it was possible to monitor and control the electrolyte wetting of the working electrode by carefully pushing it towards the separator using the manipulator. Depending on the materials investigated and size of the electrodes, electrical currents were between 100 nA and several µA.

Experiments with this method were performed on SnO_2 and CCS. The size distribution of the SnO_2 particles (99.9 % purity, −325 mesh, Sigma-Aldrich) in the electrodes was very broad with diameters ranging from tens of nanometres to several microns. The electrodes contained 10 wt. % carbon black and 10 wt. % PVDF and 80 wt. % of the electrochemically active material.

The *in situ* observation of lithium cells inside the SEM was complicated by artefacts related to the direct probing by the electron beam. During scanning, the beam hits a very small area of a few nm^2 and can lead to significant charging of the imaged region. In the open cell,

such effects can strongly interfere with battery operation and therefore have to be prevented. Most problematic in this respect is the electrolyte which is a poor electron conductor. When imaged in the SEM, it can strongly build up charge leading to unwanted effects like local lithium deposition. For imaging, it is therefore important to select regions of the battery that have both good electrical connection to the current collector and are also not covered by large amounts of electrolyte. Typically, regions close to the stainless steel mesh (Figure 19) were selected and beam currents and imaging times were minimized to avoid charging effects.

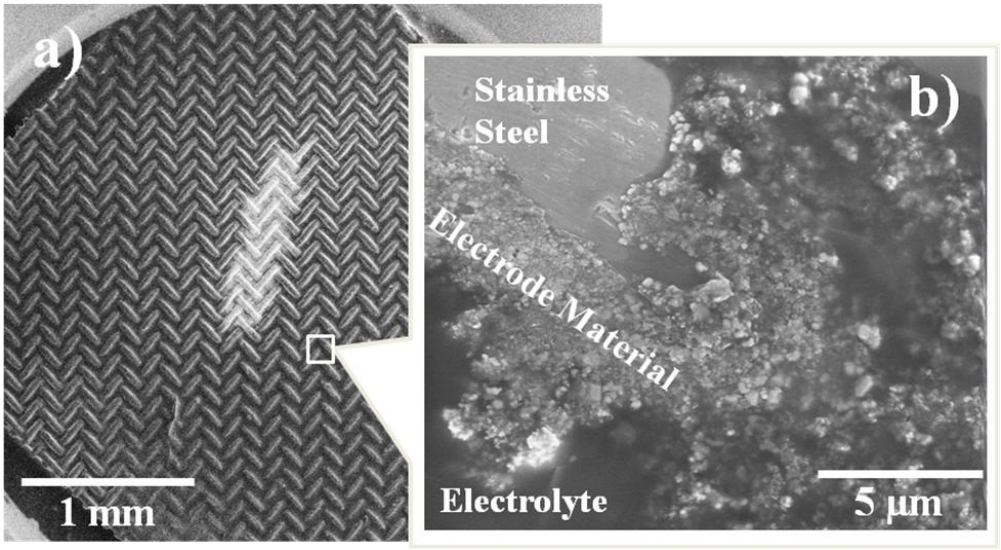

Figure 19: Using the manipulator, the working electrode can be carefully pushed towards the separator. By doing this, it is soaked by the electrolyte leading to the large dark region in image (a). Once fully soaked, regions close to the stainless steel mesh were selected for imaging in order to ensure proper grounding and to avoid electric charging effects (b).

3.4 *Ex situ* SEM experiments

Intercalation materials are currently used as active materials in the lithium-ion secondary batteries. Compared to conversion materials, they have excellent reversibility during charge and discharge, which results in a much longer cyclic life. Such systems are not applicable to *in situ* testing where the time on the microscope is limited. For this reason, a different strategy was used for investigating these materials. Electrodes with intercalation materials were electrically cycled in Swagelok-cells and *ex situ* observed at given times by SEM.

The particles of the active material under investigation were mechanically mixed with PVDF and carbon black with a ratio of 8:1:1 in weight, respectively. PVDF binder and carbon black were used to build an electron conductive matrix for embedding the active material. NMP was applied to dissolve the PVDF and make a slurry. The slurry was then coated on the aluminum substrate (99.9 % purity, 0.5 mm thick) using a film casting machine to achieve a wet film with a thickness of 120 µm. The electrode with active material, binder, carbon black and the aluminum substrate as current collector was then dried at room temperature for 24 hours and afterwards heated to 90 ℃ for at least 24 hours in atmosphere. After this step, this electrode was ready for using as a working electrode in a test cell.

1M Lithiumhexafluorophosphate ($LiPF_6$ salt) dissolved in ethylene carbonate (EC)/ dimethyl carbonate (DMC) solution (1:1 in weight, Merck battery electrolyte LP 30, water content < 20 ppm, HF (as free acid) < 50 ppm) was selected as electrolyte. The same laboratory filter paper as used in the *in situ* experiment was also used in this experiment as separator. It has a low ionic resistance and effectively prevents short circuits after thousands of cycles.

Pure lithium was used as counter electrode, so that the potential on the negative electrode was kept constant during charge and discharge. Moreover, excess lithium provided unlimited anode capacity during the experiment, so that the loss of lithium does not affect cell performance. For the current collector of the negative electrode, nickel plates (99.5 % purity, 0.25 mm thick, Alfa aesar) were used.

The cell components were assembled in a Swagelok connector with Teflon® sealing, stainless steel springs and rods to make a Swagelok-cell (Figure 20). When the Swagelok connector made from metal was used, a piece of polyethylene (PE) foil is applied to separate the battery components from the metal housing. The stainless steel spring pushed the battery components together and improved the electrical contacts. Both electrodes could be electrically connected to the battery galvanostat through the stainless steel rods. Cells of this type are common in batteries and could be easily disassembled and opened inside a glove box.

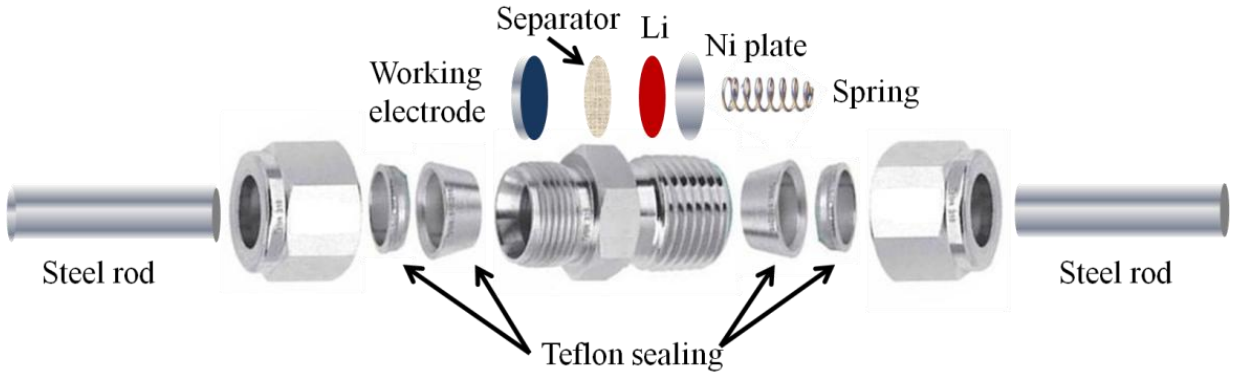

Figure 20: Setup of a Swagelok-cell for building batteries for *ex situ* SEM observation.

Several active materials: LMAO (Süd Chemie AG, Munich, Germany), LNMFO synthesized by S. Glatthaar from Institute for Applied Materials of Karlsruhe Institute of Technology, LCO (99.5 % purity, 5 micron APS Powder, Metals basis, Alfa aesar) were investigated in the *ex situ* SEM experiments. The LMAO particles investigated in this work had diameters between hundreds of nanometers and several microns with a mean particle size of 1.019 microns nm and median particle size of 0.919 micron. The size distribution of three LMAO samples was characterized by SEM and is shown in Figure 21.

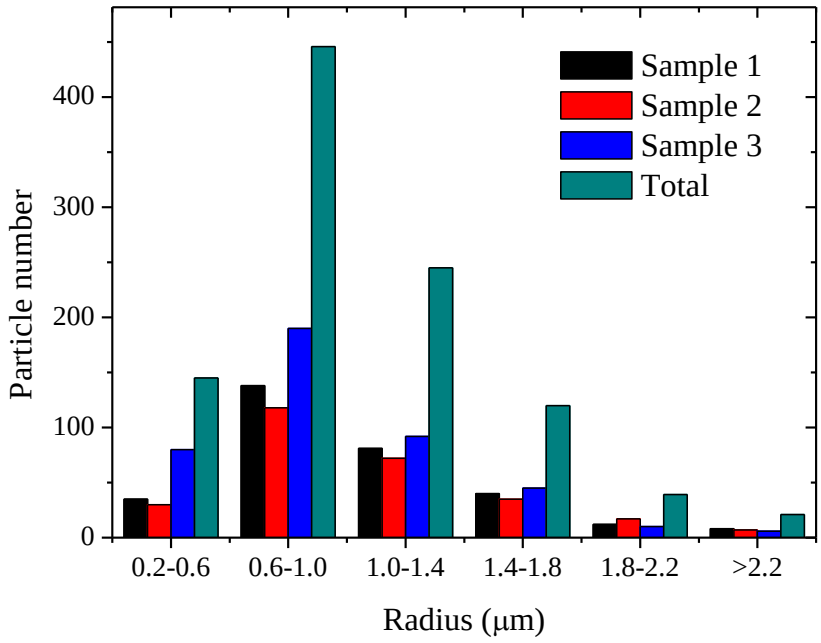

Figure 21: Size distribution of particles that were investigated in the *ex situ* experiments.

The fabricated working electrodes were imaged by SEM before the electrochemical experiments. After this step, a Swagelok-cell was assembled and tested. After a given number of cycles, the test was interrupted and the cell was disassembled in the glove-box. In order to remove residue from the electrolyte, namely $LiPF_6$ salt and EC, the electrode was washed by DMC. After drying, the working electrode was moved into the transfer container and transferred into the SEM chamber which prevented contamination by oxygen and moisture (Figure 18). After pumping to high vacuum (~ 10^{-6} mbar), the pump was turned off and the transfer container was opened by rotating the sample stage. The working electrode was imaged and attention was paid to investigating the same particles which were imaged before electrical cycling. In some cases after the inspection of the sample, the transfer container was closed again under high vacuum and the electrode under investigation was brought back to the glove-box, where the battery was reassembled for further testing. With this procedure, the working electrode and the

active material particles could be microscopically investigated at defined intervals during battery operation.

4 Results

Using the *ex situ* SEM experimental method presented in section 3.4, commercial intercalation materials for the positive electrode LMAO, LCO and LNMFO were investigated. The major finding was made in LMAO electrodes. Defects in the form of cracks were frequently observed in the active material particles after electrical cycling and the number of particles with cracks increased with rising cycle number. Further, a particle size dependence of the crack formation could be found. Details of these observations are given in section 4.1.1. Significant structural changes are expected to occur in many conversion materials during the first reaction with lithium ions. The conversion materials SnO_2 and CCS were investigated by the *in situ* SEM technique mentioned in section 3.3. Such effects will be shown in section 4.2 where the morphological evolution related to lithium insertion/extraction of the two conversion materials is addressed.

4.1 Intercalation materials

Positive electrodes with intercalation materials LMAO, LCO and LNMFO were electrically cycled in Swagelok-cells and *ex situ* investigated by SEM to detect material changes induced by cycling. Degradation could be generally measured in test cells by analyzing the voltage and capacity changes (section 4.1.1). High resolution secondary electron images of individual particles in the fabricated electrodes before and after electrical cycling show the consequences of the cyclic loads. By investigating large regions of the electrodes a relationship of damage and cycle number as well as particle size could be observed (section 4.1.1).

4.1.1 $LiMn_{1.95}Al_{0.05}O_4$

Electrical degradation

Several test cells with LMAO as the active material in the positive electrode were galvanostatically cycled. One sample was cycled at a rate of 1C for 800 cycles. Continuous capacity fading was measured during electrical charge and discharge (22, Table 2). The rate of capacity derease stayed almost constant. As a result, an almost linearly capacity fading was observed in the range of 100% to 75% of the initial capacity. The charge capacity decreased by 21 % and the discharge capacity decreased by 23 %. Details of this decrease can be found in Table 3. The capacity fading is also visible in the voltage curve in Figure 23, where the voltage changes were plotted versus lithium content x in the spinel host material. Both, during charge and discharge, decreasing amounts of lithium could be inserted and released from the host material with increasing cycle number. A voltage profile shift can be seen by comparing the 20^{th}, 100^{th}, 300^{th}, 600^{th} and 800^{th} cycle when considering the two plateaus. During charge they shifted to higher voltages and during discharge to lower voltages. In other words, with increasing cycle number more energy was needed for charging the cell, and less energy was released during discharge. Consequently the specific energy of the cell also decreased with increasing cycle number.

Table 2: Degradation of the LMAO-lithium cell with a rate of 1C after 800 cycles

	Pristine	After 800 cycles
Charge capacity ($mAhg^{-1}$)	111	88.1
Discharge capacity ($mAhg^{-1}$)	110.4	85
Coulumbic efficiency (%)	99.5	99.5

Table 3: Capacity decrease and their decreasing rates

	Capacity (%)
Decrease of charge	-20.6
Decreasing rate of charge per cycle	-0.029
Decrease of discharge	-23
Decreasing rate of discharge per cycle	-0.033
Decrease of efficiency	-3.5
Decreasing rate of efficiency per cycle	-0.0045

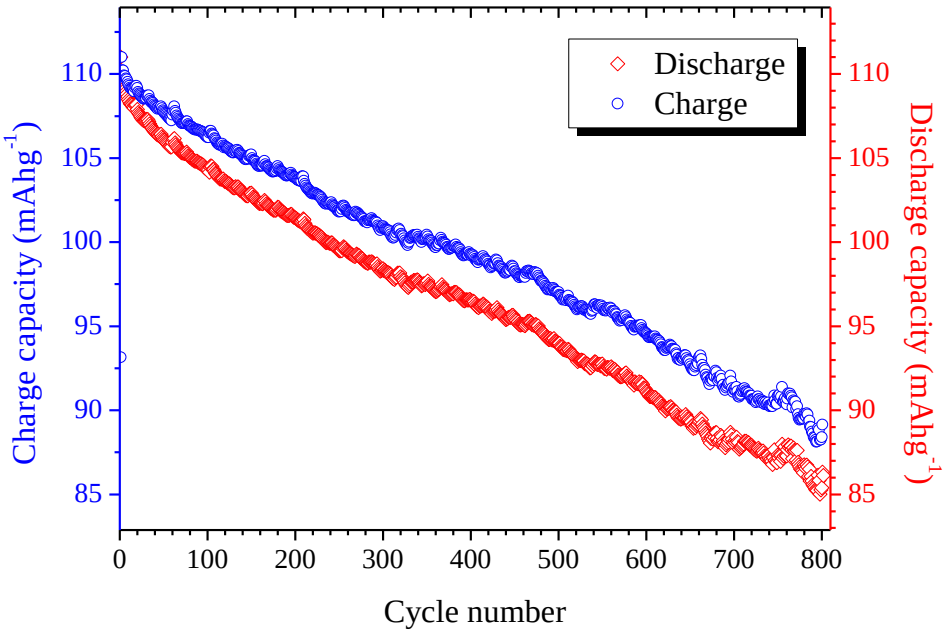

Figure 22: Capacity degradation of the LMAO-lithium cell cycled with a rate of 1C.

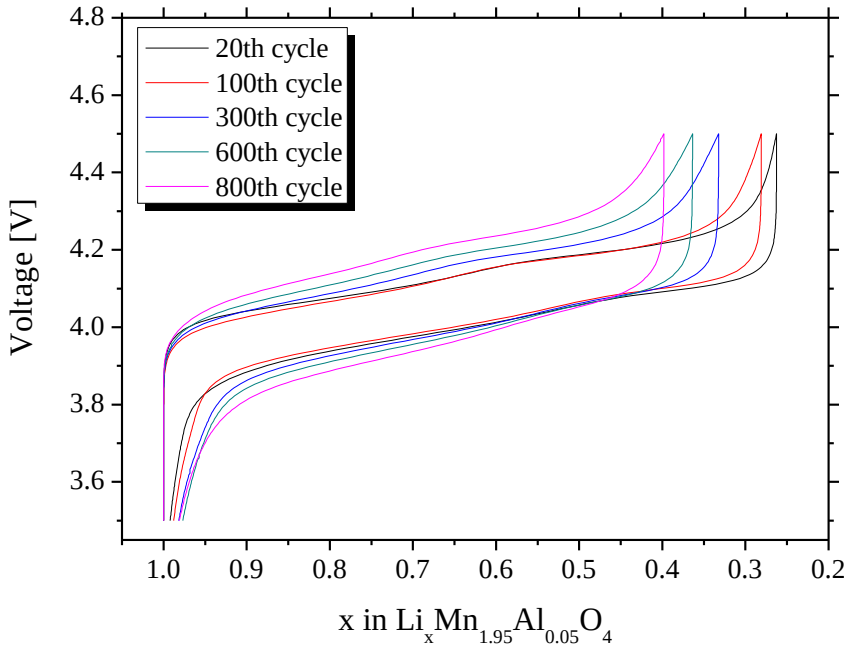

Figure 23: Voltage profile of the LMAO-lithium cell with increasing cycle number.

Microscopic observation

After electrical operation, the Swagelok-cells were disassembled and their working electrodes were transferred to the SEM chamber for observation. Several locations in the working electrode were imaged by SEM. These images after a given number of cycles were then compared with those images made before electrochemical intercalation for detecting morphological changes.

Figure 24 shows LMAO particles embedded in the electron conductive matrix consisting of binder and carbon black. This sample was cycled at a rate of 5C for 1015 cycles. The observation shown in Figure 24 is characteristic for the electrodes tested here. After a few hundreds of cycles, the binder had moved and gaps between the active particles and the PVDF

became visible. The small features on top of the active material in Figure 24b are most likely due to residual $LiPF_6$.

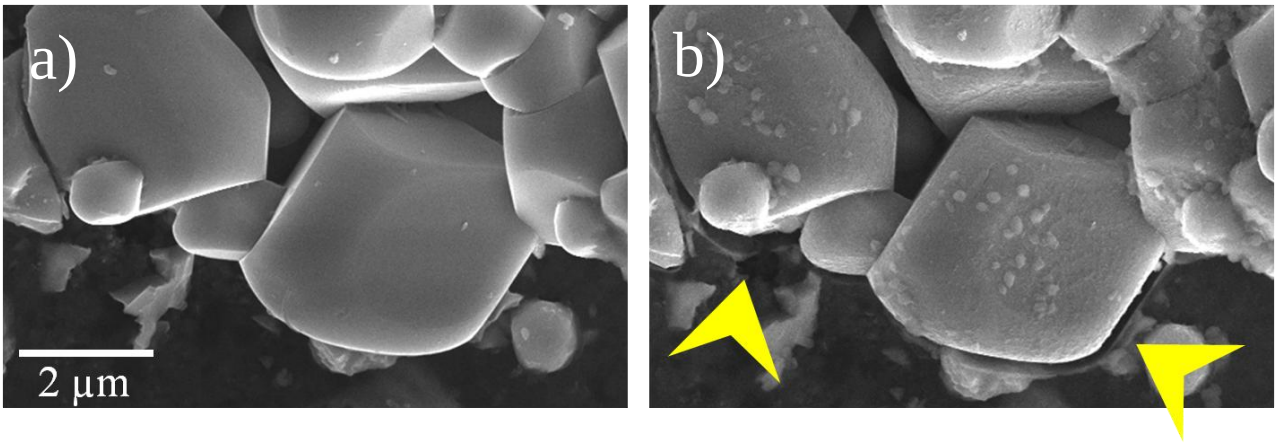

Figure 24: Gaps as marked by the arrows between LMAO particles and matrix were found by comparing (a) the sample before electrochemical intercalation and (b) the same sample after 1015 cycles.

Besides the disconnection between active material particles and matrix, cracks were observed on the LMAO particles surface after a given number of cycles. The as-received LMAO spinel had a voltage of 3.2 V versus lithium in the electrochemical cell. At 3.2 V, the factor x in $Li_xMn_{1.95}Al_{0.05}O_4$ approaches 1. During the first charge, the cell voltage increased from 3.2 V to 4.5 V. During charging, the lithium ions and the corresponding electrons were extracted from the spinel lattice. The first cracks were observed on the surface of a few particles after the first electrochemical lithium extraction from LMAO particles (Figure 25b). These cracked particles were among the largest particles that could be found in the electrode.

After the first SEM observation in the fully charged state, the sample was discharged to 3.5 V in the electrochemical cell. The lithium ions were electrochemically inserted into the spinel host material for the first time. The images taken after the first discharge show that some cracks that had formed during the first charge grew along the same orientation (Figure 25c). Additionally, new cracks also formed during the first discharge of the cell (Figure 26).

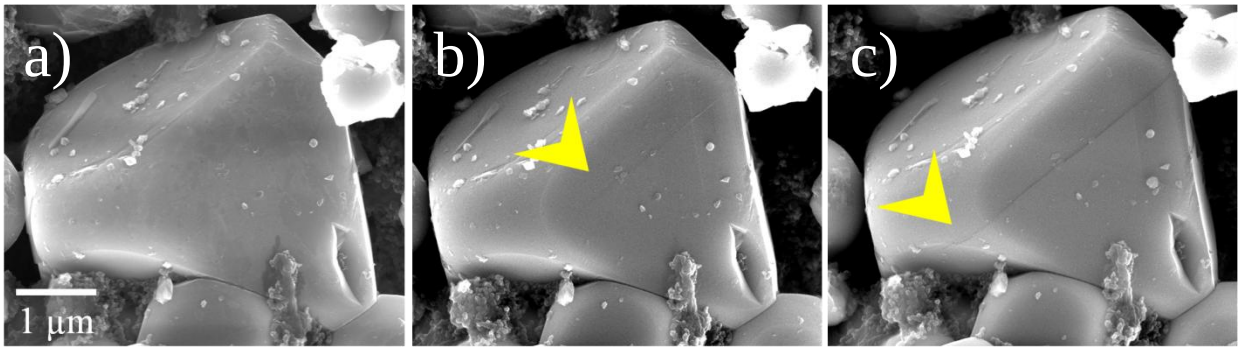

Figure 25: LMAO spinel particle (a) in pristine, (b) after the first charge (lithium extraction) and (c) after the first discharge (lithium insertion). Micro-cracks formed during the first electrochemical lithium extraction and some of these cracks grew along the same orientation during the subsequent first lithium insertion.

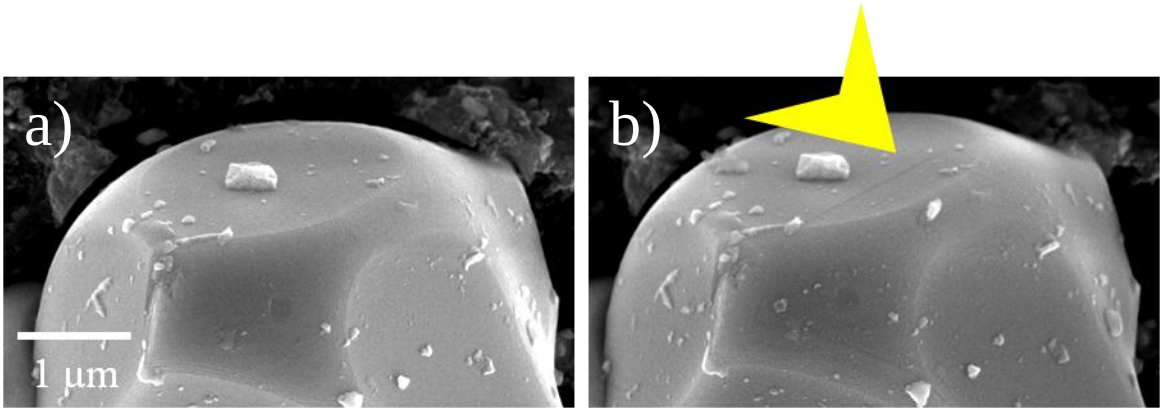

Figure 26: LMAO spinel particle (a) after the first charge (lithium extraction) and (b) after the first discharge (lithium insertion). A crack nucleated and grew during lithium insertion.

Crack formation and mechanical damage became more extensive with increasing number of cycles. Figure 27 shows damage on a LMAO particle after 800 cycles at 1C rate. As shown in this image, for some instances, a small part of the active material broke off from the particle (Figure 27b). The mechanical damage includes not only brittle cracking, but also material deformation. Figure 27b shows a trace of deformation in the form of band structure on the surface of the LMAO particle. Band structures with a width of ~ 300 nm formed on the particle surface are distinct in the magnified image (Figure 27c). Fine cracks can be repeatedly found along the edges of the band structures. Figure 27d shows the same location as Figure 27a

recorded at different rotation and tilt so that the electron beam runs almost parallel to one of the facets of the particle. In this image a step of ~ 30 nm becomes apparent on the particle surface which shows that the band structures are associated with a shear process.

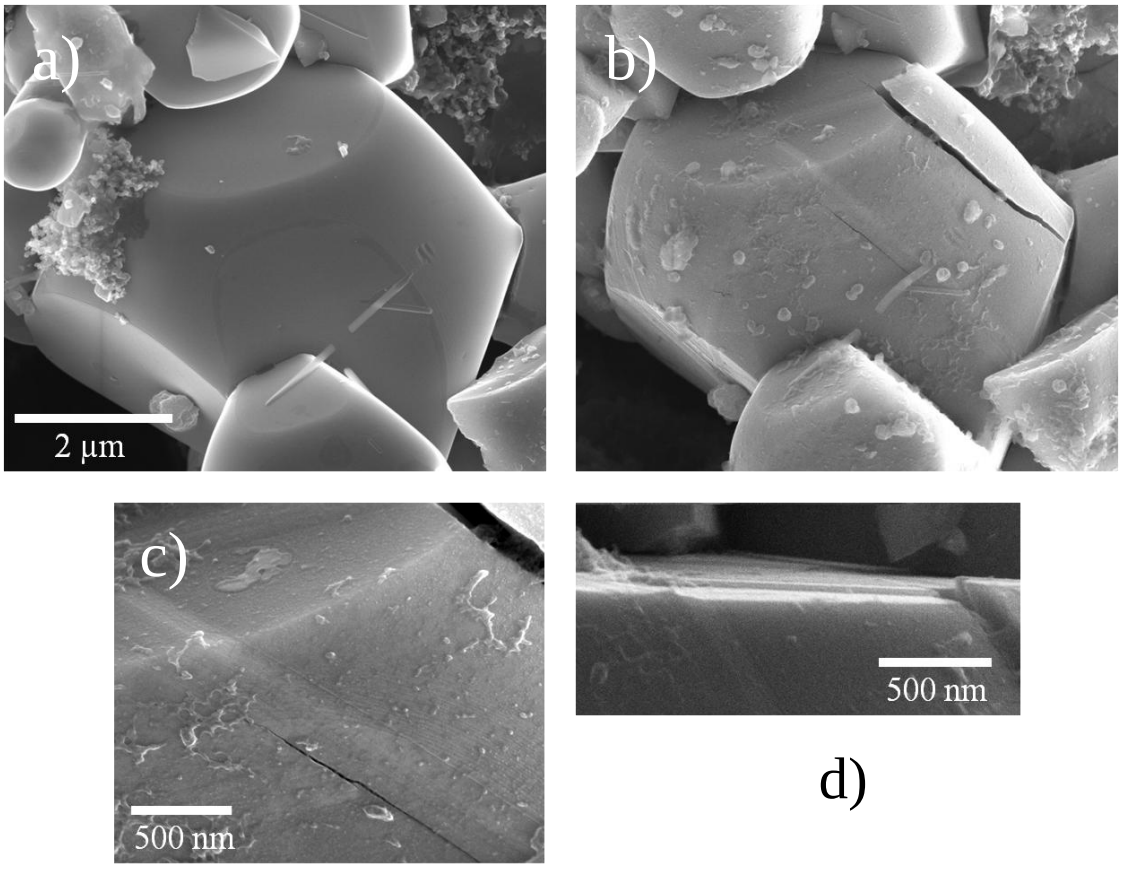

Figure 27: Images of a LMAO spinel particle in (a) pristine state, (b) after 800 cycles, (c) magnified region of (b), (d) specimen tilted and rotated to show the sheared particle.

Often cracks were found in the proximity of the band structures (Figure 28a) but most of the cracks were not located at bands. In particular for smaller cycle numbers, no bands were found but cracks were detected. Most cracks showed a given symmetry. Figure 28b shows a particle with three cracks in 120 °rotational symmetry. This shows that the surface containing the cracks is a {111} plane. In Figure 28b, the {111} surface is almost parallel to the plane of the image. In order to gather information from the inside of the particles, several particles were

sectioned layer by layer in a focused ion beam microscope (FIB). It was found that cracks were also present inside the particles and that not all cracks had reached the particle surface (Figure 28c). Cracks inside the particles became visible by imaging the cross-section of these particles. In the layer by layer sectioning it was observed that many crack surfaces are not perpendicular to the sample surface but instead are inclined at an angle so that the surfaces of the cracks are parallel to the sidewalls of the particle. This indicates that many of the observed cracks run along {111} planes (Figure 29).

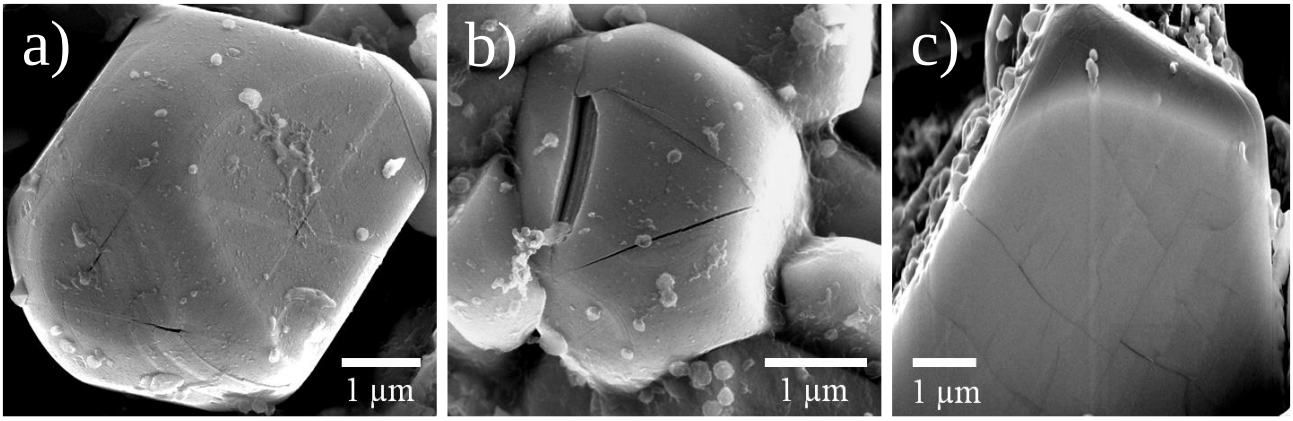

Figure 28: (a) Cracks next to deformation bands. (b) Threefold symmetry of cracks. (c) Cracks inside a particle. Image (c) was taken at 52 ° tilt angle relative to the cross sectioned surface (image was stretched to correct for tilt).

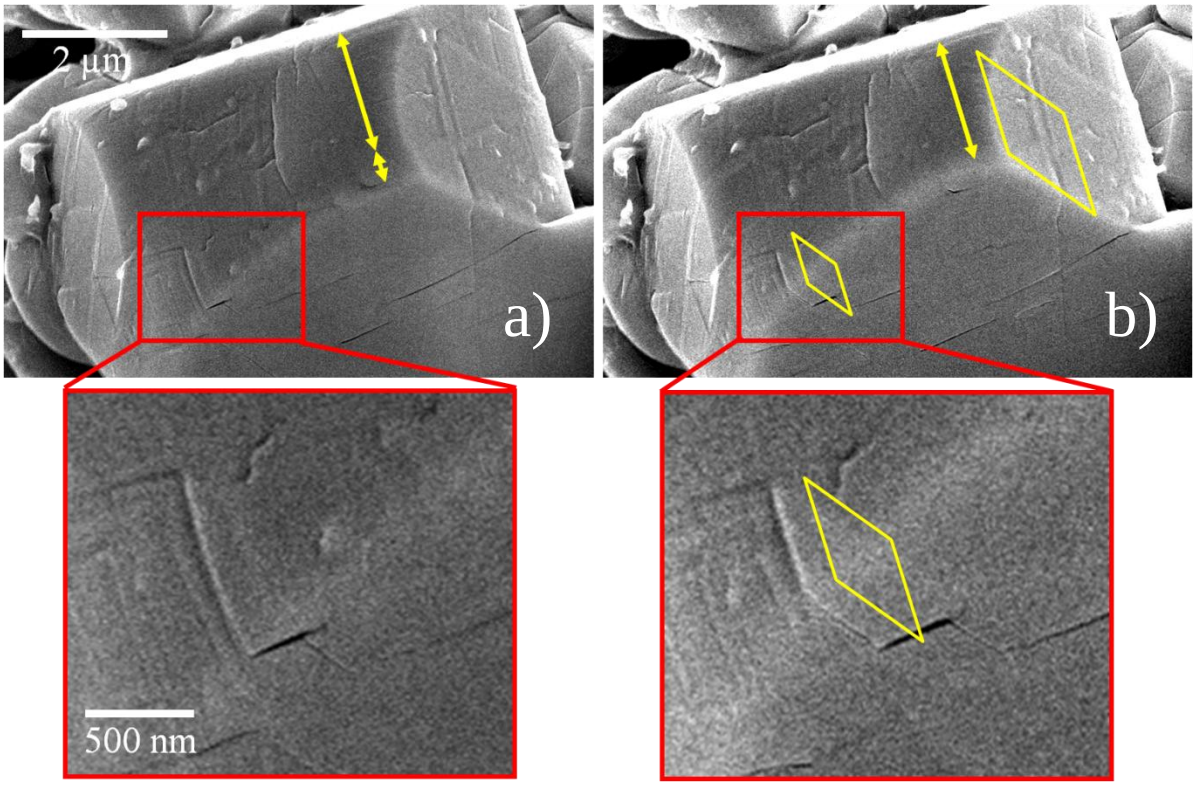

Figure 29: By means of FIB, some particles were sectioned layer by layer, (a) initial and (b) after one section. The two dimensional orientation of one crack can be determined from the lines of intersection between the crack, the cross-section and the surface. It seems that the cracks prefer the {111} direction parallel to the surface plane of the cubic crystal.

In order to obtain statistical data on these phenomena, randomly selected areas on the working electrode were imaged in high resolution. Several hundred of LMAO particles were included within an image area of 0.01 mm^2. Using pixel counting in the images, the two-dimensional projected area of every particle was calculated. The one- dimensional radius of the particles was estimated from the projected areas under the assumption that the particles were spherical. The particles with cracks on their surfaces were marked. A crack ratio could then be calculated from the number of cracked particles and the number of all analyzed particles. Three samples were analyzed by this method. The first sample was cycled at 3C rate for 200 cycles. The second one and the third one were cycled at 1C rate for 200 cycles and 800 cycles, respectively. The ratios of cracked particles were different in all three samples as shown in Table 4, Table 5 and Table 6.

The particles analyzed in these three samples had no uniform size, but radii ranging from several microns to hundreds of nanometres. They were classified in six ranges: namely larger than 2.2 microns, from 1.8 to 2.2 microns, 1.4 to 1.8 microns, 1.0 to 1.4 microns, 0.6 to 1.0 microns and 0.2 to 0.6 microns. Particles with different sizes had also different individual crack ratios in all three samples. The dependence of crack ratio to the particle size is shown in Table 4, Table 5 and Table 6. The average crack ratio of the three samples independent to the size distribution was 0.351 (Sample Nr.1), 0.337 (Sample Nr.2) and 0.468 (Sample Nr.3), respectively. To better understand this size effect, the individual crack ratio is plotted versus the particle radius in Figure 30.

In every sample, smaller particles had a lower crack ratio and this effect was almost linearly related to the calculated one-dimensional particle radius. The particles with radii larger than 2.2 microns had a high crack ratio of 0.875 in the first sample and 0.857 in the second sample. In the third sample the calculated crack ratio reached even 1, which means every particle in this range had cracks on its surface. In contrast, the particles with radii smaller than 0.6 micron had a fairly low crack ratio of 0.038 in the third sample and 0 in the first and the second sample.

Table 4: Statistics of crack formation in Sample Nr.1 cycled at 3C for 200 cycles

Radius range (μm)	Number of particles	Number of particles with cracks	Ratio
0.2-0.6	35	0	0
0.6-1.0	138	6	0.043
1.0-1.4	81	14	0.173
1.4-1.8	40	14	0.350
1.8-2.2	12	8	0.667
>2.2	8	7	0.875
Total	314	49	0.156

Table 5: Statistics of crack formation in Sample Nr.2 cycled at 1C for 200 cycles

Radius range (µm)	Number of particles	Number of particles with cracks	Ratio
0.2-0.6	30	0	0
0.6-1.0	118	8	0.068
1.0-1.4	72	12	0.167
1.4-1.8	35	12	0.343
1.8-2.2	17	10	0.588
>2.2	7	6	0.857
Total	279	48	0.172

Table 6: Statistics of crack formation in Sample Nr.3 cycled at 1C for 800 cycles

Radius range (µm)	Number of particles	Number of particles with cracks	Ratio
0.2-0.6	80	3	0.038
0.6-1.0	190	23	0.121
1.0-1.4	92	36	0.391
1.4-1.8	45	25	0.556
1.8-2.2	10	7	0.700
>2.2	6	6	1
Total	423	100	0.236

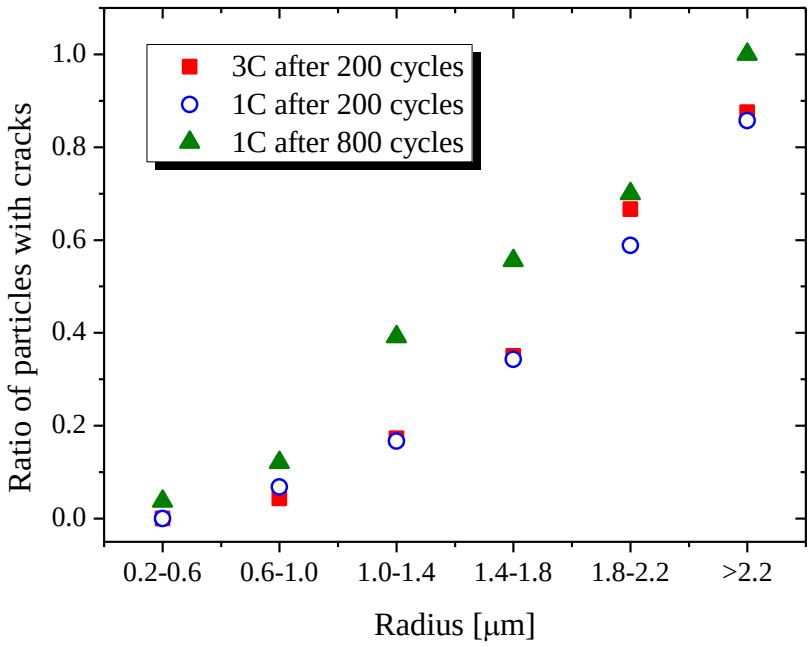

Figure 30: The crack ratio of LMAO particles for different rate, cycle number and particle size.

In a long-term experiment, one working electrode with the same LMAO was charged to 4.5 V in a Swagelok cell and stored under the same conditions for 2 months. Thereafter, no cracks were found on the LMAO particle surface by means of SEM.

4.1.2 $LiCoO_2$ and $LiNi_{0.4}Fe_{0.1}Mn_{1.5}O_4$

The active materials LCO and LNMFO were also investigated in the *ex situ* SEM battery experiments. One sample with an LCO electrode was galvanostatically charged and discharged in a Swagelok-cell between 3.5 V and 4.2 V at a rate of 2C for 220 cycles. Another sample with LNMFO electrode was galvanostatically cycled between 3.5 V and 5 V at a rate of 2C for 986 cycles. Both Swagelok-cells demonstrated continuous capacity fading and voltage plateaus shift as shown in Figure 31 and Figure 32. With increasing cycle number, the charge plateaus were

shifted to the higher voltage range, while the discharge plateaus moved to the lower voltage ranges.

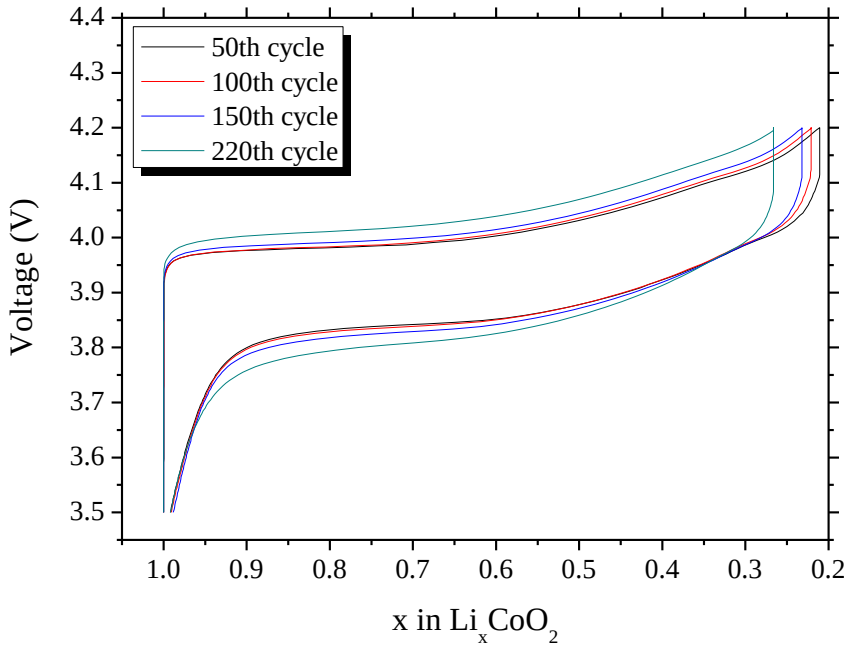

Figure 31: Voltage profile of the LCO-lithium cell with increasing cycle number.

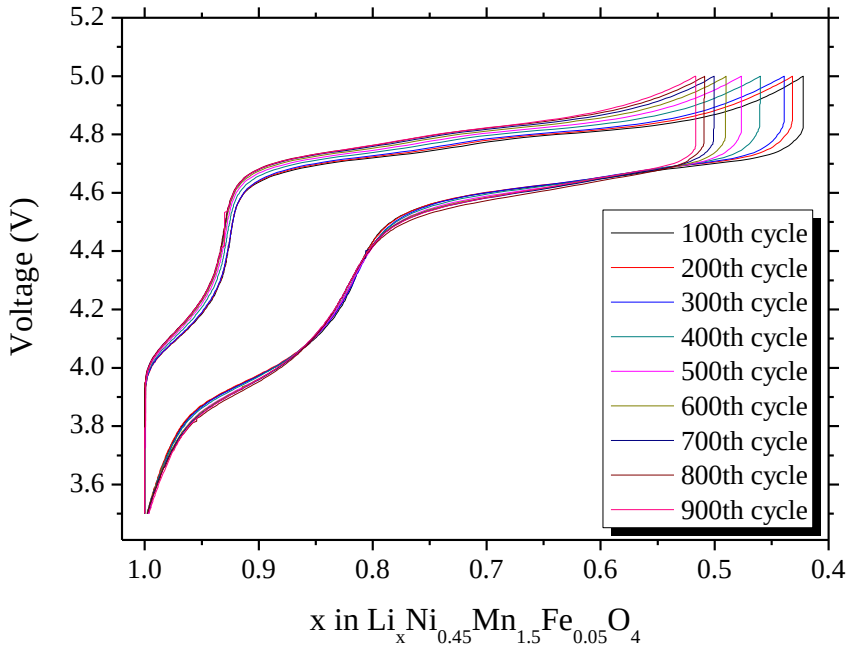

Figure 32: Voltage profile of the LMNFO-lithium cell with increasing cycle number.

More than 20 active material particles in the fabricated LCO and LNMFO electrodes were imaged with SEM before electrochemical lithium insertion/extraction. After the cycling, the Swagelok-cells were disassembled. The working electrodes and the same particles were observed again. No cracks or other significant morphological changes could be detected in the two materials.

4.2 Conversion materials

The conversion materials SnO_2 and CCS showed large capacities for lithium storage in the test cells, which decreased rapidly after the first few cycles. *In situ* SEM observation during electrochemical lithium insertion and extraction showed local changes such as volume expansion, crack formation, extrusions. SnO_2 was also investigated by *ex situ* SEM for proving the results of the *in situ* SEM observation (section 4.2.2). The observations help to better understand the reaction pathways of both materials and the rapid degradation of SnO_2 and CCS.

4.2.1 $CuCr_2Se_4$

The CCS powder used for the experiments was synthesized by W. Bensch et al.. Details about this material can be found in [62]. For the in situ SEM experiment, the powder was mixed with binder and carbon black to produce a working electrode. The method is described in more detail in Chapter 3. The CCS-lithium cell inside the SEM chamber had a voltage of ~3.0 V after assembling. This cell was galvanostatically discharged to 0.4 V. During the discharge, lithium was inserted for the first time. The voltage profile with constant discharge current is shown in Figure 33. Three discharge plateaus were observed at 1.6 V, 1 V and 0.6 V versus lithium.

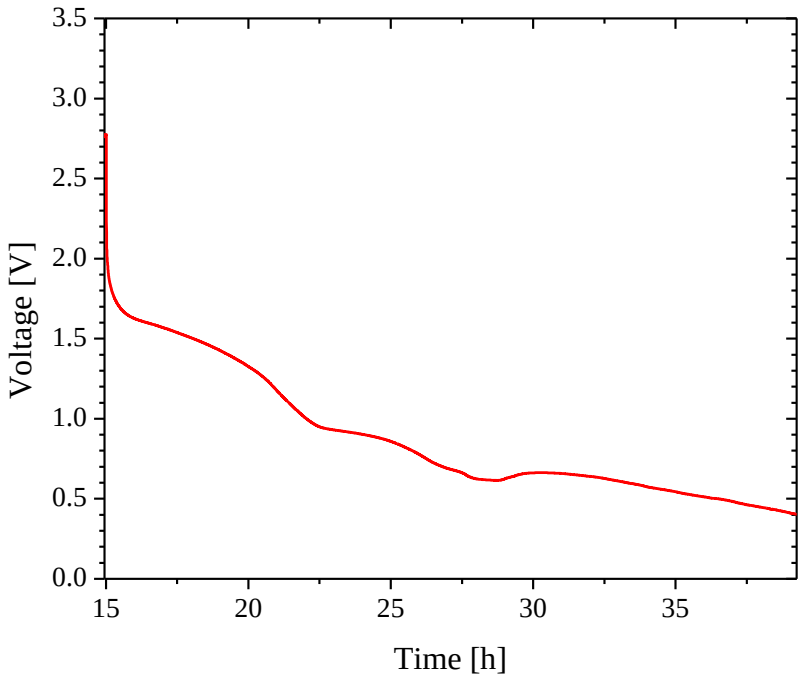

Figure 33: Voltage profile of the *in situ* cell inside SEM with CCS as working electrode and lithium as counter electrode.

Significant morphological changes could be determined by comparing the SEM images of CCS particles at different SOC. During the real-time observation, it was found that cracks and wires like extrusions formed during lithium insertion. Several CCS particles were selected to be continuously monitored during the discharge process (Figure 34). In this way, the relationship between the observations and the SOC was assured. Starting at 3 V and decreasing, a first change was found at 1.458 V. Here the first extrusion was observed on the particles. The extruding process continued only until 1.306 V. At 1.094 V, the first crack was observed on the surface of a particle. More cracks formed until 0.944 V. After that no significant change was detected anymore. After the first discharge, the cell was charged with the same current and subsequently cycled between 2.9 V and 0.4 V. Compared to the first discharge, the capacities of the following charges and discharges were significantly smaller and no further morphological change was detected.

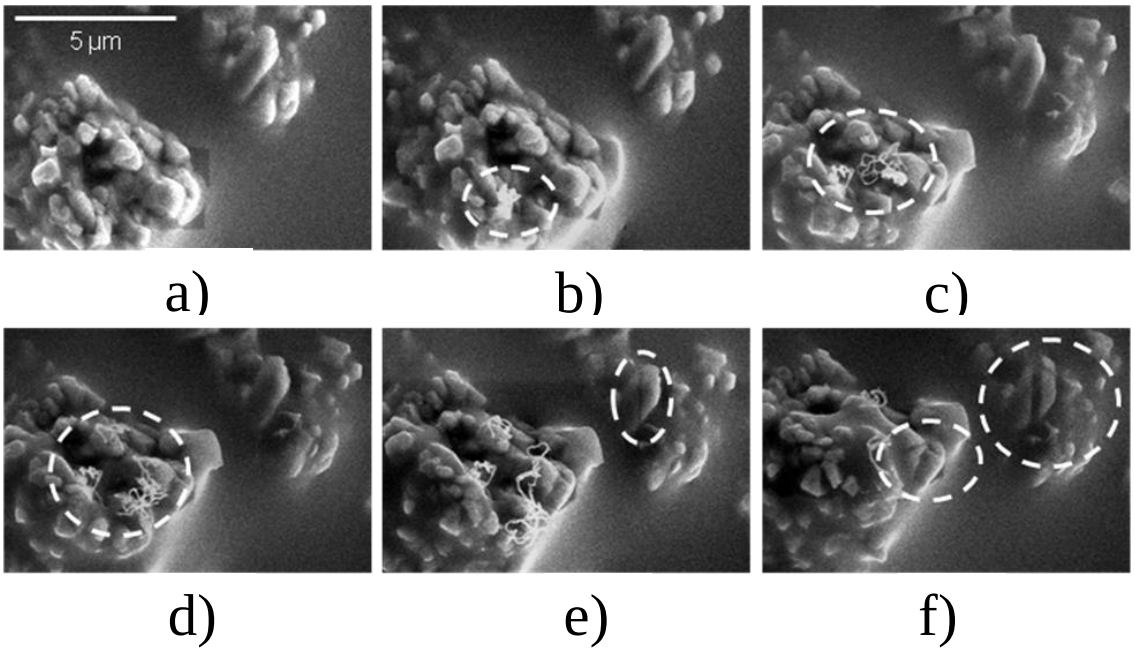

Figure 34: *in situ* SEM observation of CCS particles during the first lithium insertion at a) 1.595V, b) 1.458V (first extrusion), c) 1.363V (more extrusion), d) 1.306V, e) 1.194V (first crack) and f) 0.944V (additional cracks).

4.2.2 SnO_2

Electrical measurement

The SnO_2 electrode was first tested in a Swagelok-cell with ionic liquid based electrolyte (see Chapter 3). In this test cell, excessive lithium metal was used on the negative electrode side. After assembling, the cell was discharged from 3.0 V to 0.02 V at constant current. Three stages could be recognized from the voltage profile (Figure 35). In the first stage, the cell voltage falls rapidly to ~1 V. A voltage plateau could be found around 1 V. In this stage, a large capacity per unit voltage was measured. After the plateau, the cell voltage drops continuously with a nearly constant slope. In this third stage between 0.9 V and 0.02 V, the cell also demonstrated a large capacity, which is almost twice of that of the second stage. After the first discharge, the test cell

was galvanostatically cycled between 0.02 V and 3.0 V. Rapid capacity fading was observed, as shown in Figure 36.

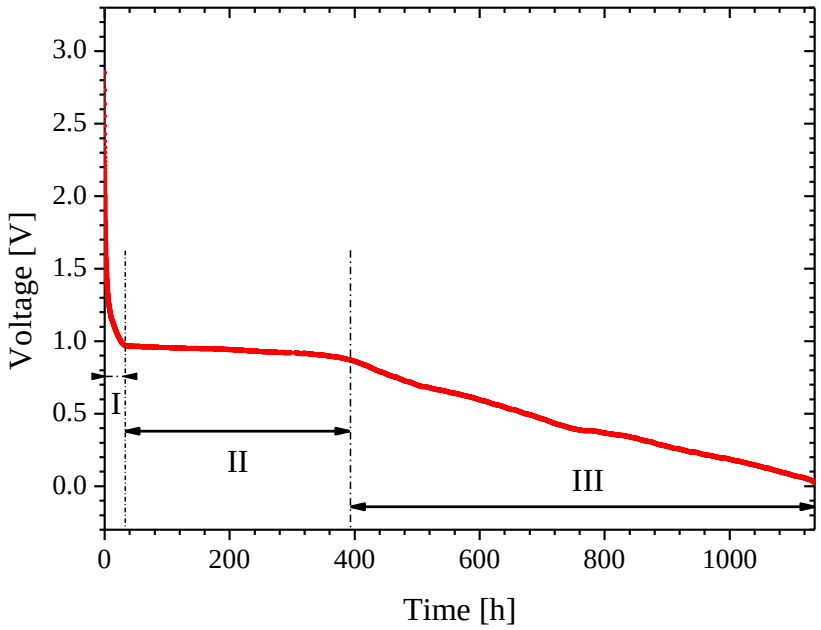

Figure 35: Three stages could be determined in the voltage profile of SnO_2-lithium Swagelok-cell during the first discharge.

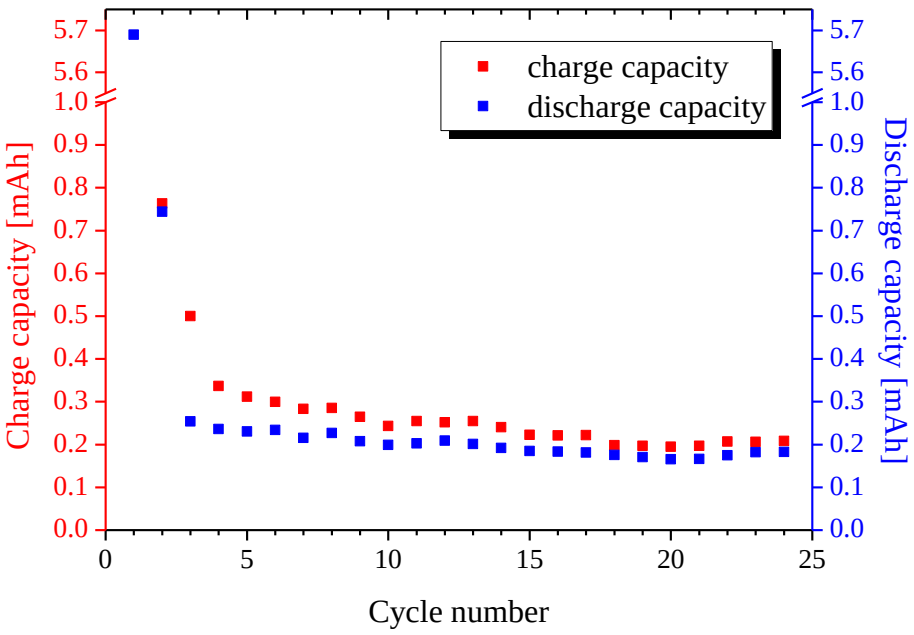

Figure 36: Rapid capacity fading of the SnO_2-lithium Swagelok-cell was measured by cycling between 0.02 V to 3 V with constant current.

The SnO_2 particles from the same batch were used in the *in situ* SEM battery experiments. The *in situ* cell was cycled under constant current between 0.02 V and 3 V. The voltage profile is shown in Figure 37. Several effects could be identified by monitoring different locations in the electrode as shown in the next section. The effects that are presented here have been repeatedly observed so that it can be assumed that these observations are representative for what is occurring inside the electrode.

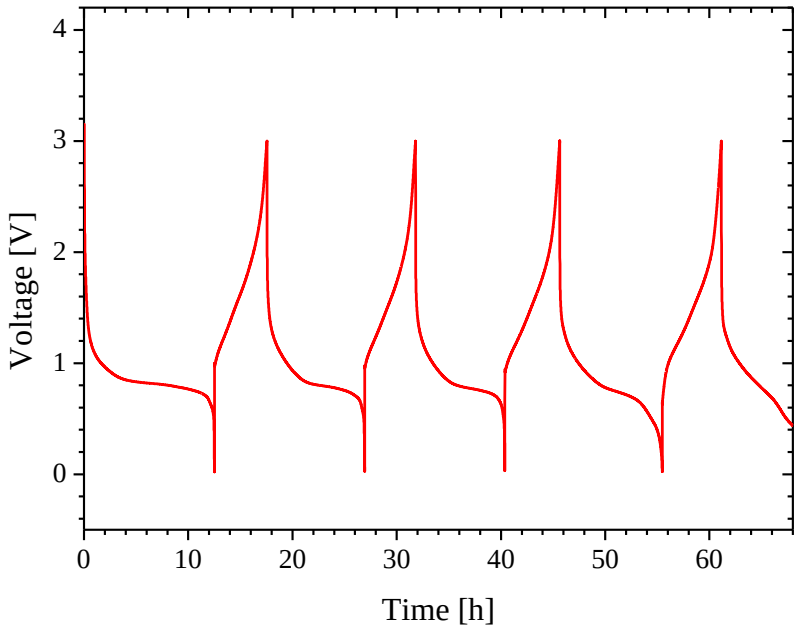

Figure 37: Voltage profile of the *in situ* SnO_2-lithium cell inside the SEM under constant current.

In situ SEM observation

A region of the electrode containing small particles with dimensions below 100 nm is shown in Figure 38. Upon the first insertion of lithium into the SnO_2 particles, the volume of the particles increased dramatically. It may be assumed that the changes in volume are more or less isotropic so that the three-dimensional volume changes can be estimated from the two-dimensional area changes. The smallest particles showed volume expansions of more than one order of magnitude. The increase in particle size occurred within the first few cycles with the change that happened within the first cycle being the largest one. At times when lithium was removed, no growth or shrinkage could be seen. Depending on imaging conditions, brighter and darker regions could be identified on the particles. During the first few cycles, the darker shell increased in thickness and then stabilized. The brighter part in the centre of the particles slightly decreased in size over the course of several cycles.

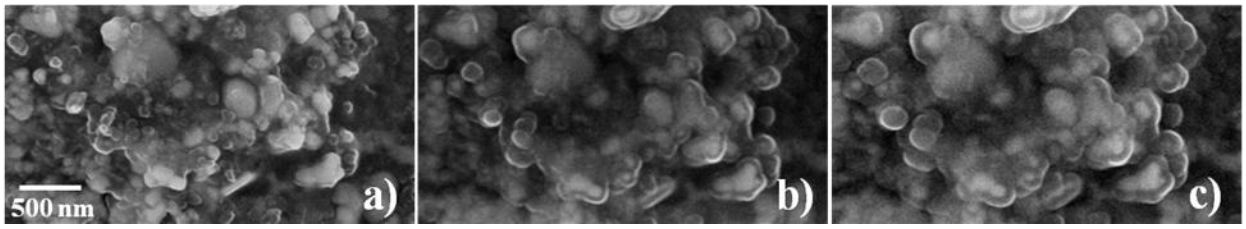

Figure 38: A section of the SnO_2 in the fabricated electrode (a) before lithium insertion, (b) after the first lithium insertion, (c) after the second lithium insertion. The micrographs have the same magnification.

On the larger particles, different effects were observed. These particles also showed a strong increase in size as can be seen from Figure 39. This increase was accompanied by a blurring of the edges and a rounding of the corners. Shells as observed on the smaller particles did not seem to form. Although the volume increase was significant, the relative volume increase was smaller than that of the small particles as can be seen by comparing Figure 38 with Figure 39. This volume increase was observed to be irreversible. In the larger particles, cracks and extrusions were observed quite frequently (Figure 39 and Figure 40) whereas no crack and extrusion were seen in the smaller particles. In the SEM, the extrusions appeared to be brighter than the particles themselves. Formation of extrusions was only observed when lithium was inserted. During lithium extraction, these extrusions kept unchanged. Almost all of the extrusions formed during the first discharge where lithium was inserted for the first time and only few of them formed during later cycles. A few of them kept growing. One extrusion after the first lithium insertion and after the 16 more cycles is compared in Figure 41. The extrusion did not grow in length; however the diameter of the extrusion became larger at its base.

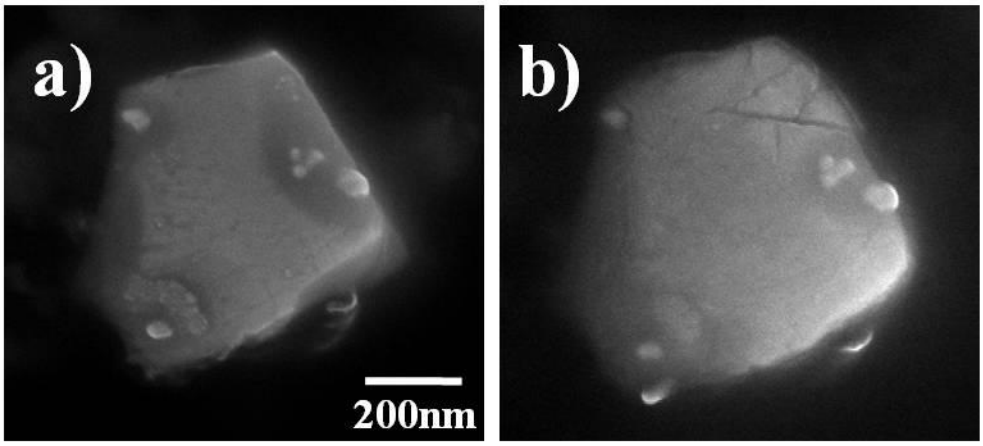

Figure 39: Single SnO_2 particle (a) before and (b) after the first lithium insertion. Besides the volume expansion, cracks and extrusions (lower left) appear on the particle surface after the first lithium insertion.

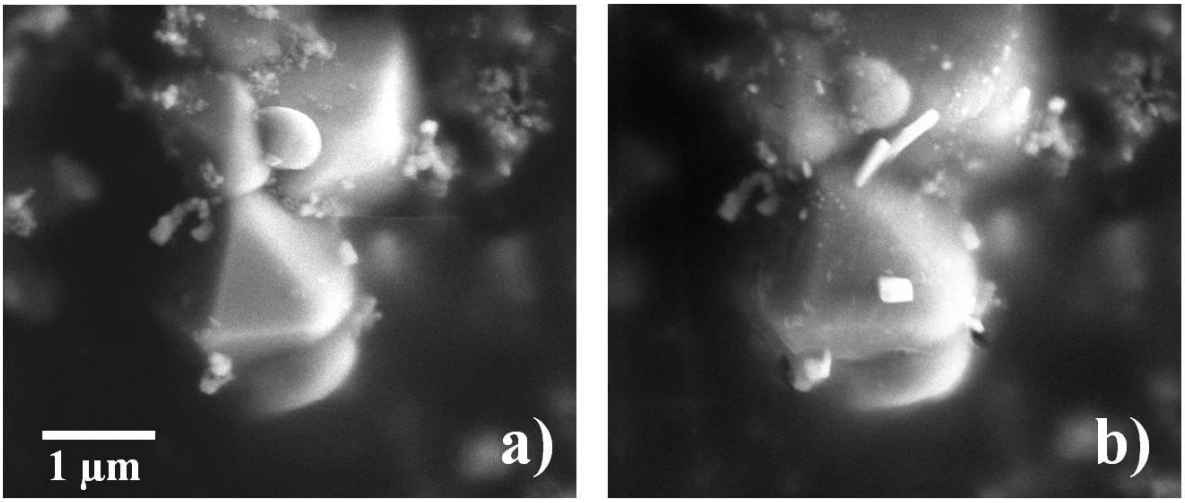

Figure 40: SnO_2 particles in (a) pristine state and (b) after the first lithium insertion. Besides the significant volume expansion and extrusion formation, the edges of the particles became blurred.

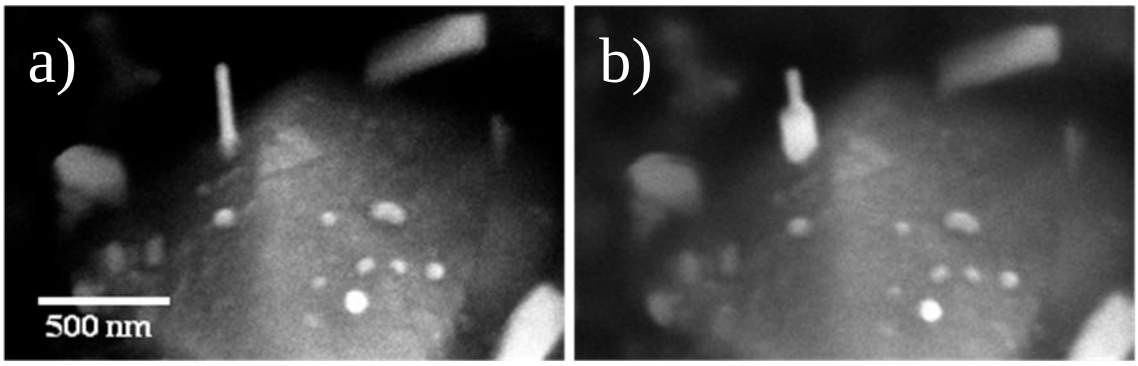

Figure 41: One extrusion appeared (a) after the first lithium insertion and (b) became larger at its base after 16 more cycles.

Although the observations that are presented here were made at the top of the electrode at regions that were not fully covered by the electrolyte, the same or similar processes also occur underneath the electrolyte level (Figure 42). Thin layers of the electrolyte are electron transparent at high accelerating voltages. It was confirmed that the described processes also take place underneath the electrolyte level.

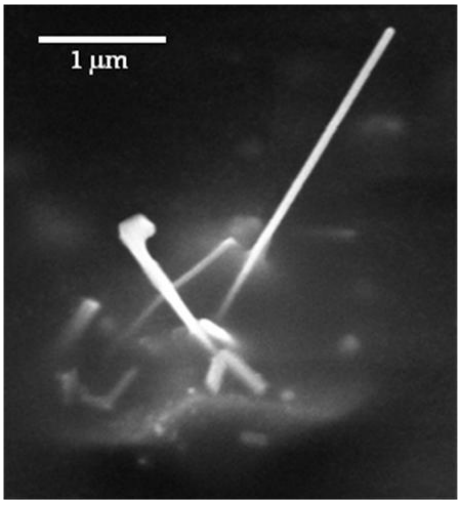

Figure 42: Extrusion grew from particles underneath the electrolyte level.

In a preliminary experiment, the growth of extrusions was monitored in real time. During lithium insertion a platelet was observed to form on a large particle. Upon lithium insertion which occurred in the course of 4 hours, the thickness of this platelet was observed to increase by

~ 50 nm within 30 min (Figure 43). This observation was made while the voltage of the electrode was between 1.1 V and 1.0 V.

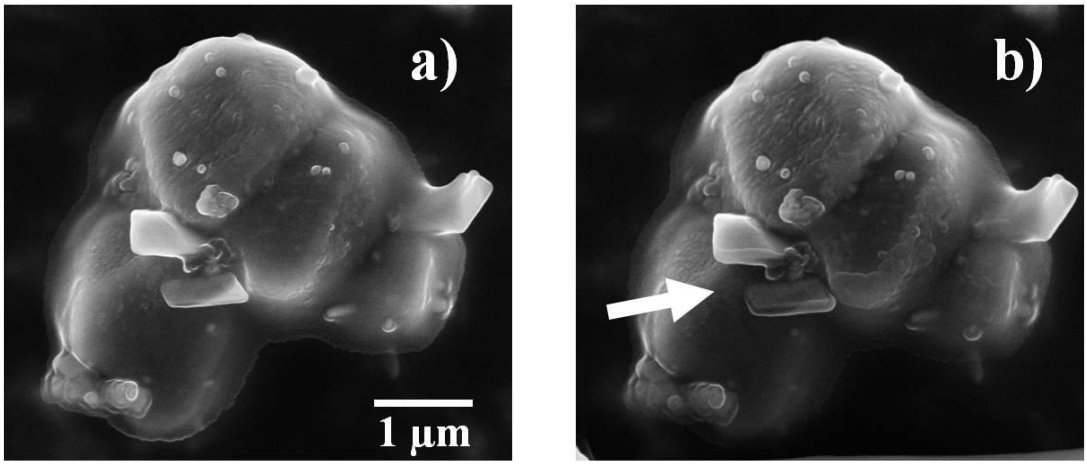

Figure 43: An extrusion was observed to grow in thickness in real time during lithium insertion.

Ex situ SEM observation

SnO_2 electrodes were also investigated within *ex situ* SEM experiments. Several SnO_2 particles in a fabricated electrode were imaged by SEM prior to electrochemical lithium insertion (Figure 44a). A Swagelok-cell with this working electrode was discharged from 3.0 V to 0.3 V at a rate of C/100 during the initial discharge. A similar voltage profile as shown in Figure 35 was detected. At 0.75 V the discharge was interrupted and the test cell was disassembled in the glove-box. The same SnO_2 particles as identified earlier in the working electrode were imaged by SEM for the second time (Figure 44b). After that, the working electrode was discharged to 0.3 V in the Swagelok-cell with moderate voltage drop. Figure 44c shows the morphology of the same particles discharged to 0.3 V. By comparing these images, similar effects observed in the *in situ* battery experiments were confirmed by the *ex situ* SEM observation. The estimated volume of the SnO_2 particle increased significantly during the first lithium insertion. The large particle shown in centre of Figure 44 expanded by a factor of 1.9 at 0.75 V and a factor of 2.8 at 0.3 V. Material extruding from the particles could already be observed after the first interrupt at 0.75 V.

However extrusions were only observed on particles that had sizes larger than several hundred nanometres.

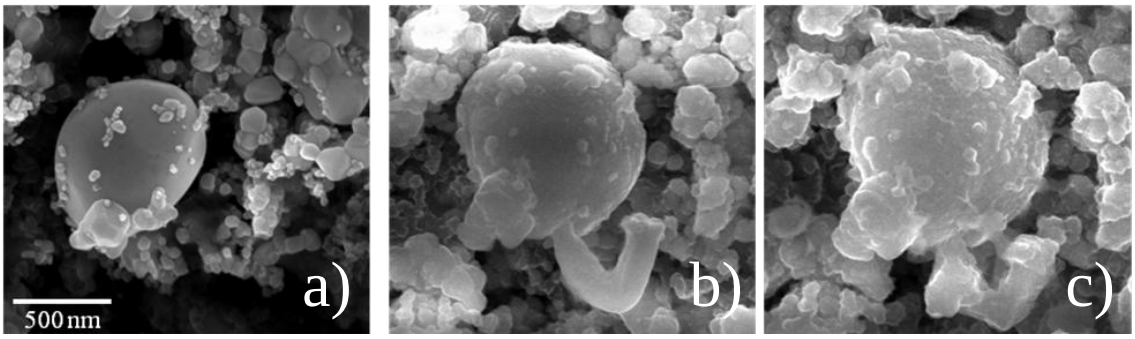

Figure 44: SnO_2 particles (a) before lithium insertion, (b) after the first lithium insertion to 0.75 V versus lithium and (c) after the first lithium insertion to 0.3 V versus lithium.

5 Discussion

Reversible lithium insertion/extraction causes cyclic mechanical stresses in the host material. Crack formation in the LMAO particles as observed in the *ex situ* SEM experiments is presented in the last chapter and is a result of such stresses. This cycling dependent material damage leads to cell degradation in capacity and in resistance. Additionally, the nature of the investigated LMAO particles and the inhomogeneous lithium insertion process leads to a size effect of the crack formation. Mechanism of the cycle number and particle size dependent mechanical damage is discussed in detail in section 5.2. The damages of conversion materials SnO_2 and CCS that are investigated in this work are different compared to that of LMAO. It is explained by the substitution reactions between the conversion materials and lithium (section 5.1). A better understanding of the damage mechanisms helps to design electrodes with better reliability.

5.1 Conversion materials

5.1.1 $CuCr_2Se_4$

Successful lithium insertion in CCS demonstrates that this compound can be used as electrode material in lithium cells. The i*n situ* microscopic study on CCS–lithium cells has shown several reaction details of lithium insertion in this spinel material. During galvanostatic charge and discharge, the capacity shown in the first discharge was much larger than those of the following charges. This means that most of the lithium reacts irreversibly with CCS during the first insertion and only a small fraction of lithium (about 20%) could be removed reversibly. The capacities shown in the sequent cycles were almost constant. Three regions with reduced slopes were observed in the voltage profile during the first lithium insertion. They indicate that different reactions or phase changes occurred during the first discharge.

In the SEM observations, different morphological changes were found in three steps during the first lithium insertion. Material extrusion could only be observed during the first step

(1.6V ~ 1.3V). The formation of cracks occurred between the first step and the third step. After that, no remarkable change was found in the third step and in the subsequent cycles.

In *in situ* XRD measurements that were performed parallel to this work, it was found that after the first intercalation reaction, elemental Cu was formed in CCS electrode in the early stage of lithium insertion[62]. Material extrusion was observed in the same voltage range in the *in situ* SEM battery experiment. These results indicate that Cu(+) was probably substituted by Li(+) to form $Li_xCu_{(1-x)}Cr_2Se_4$ and metallic Cu, which was extruded from the particles. According to the *in situ* SEM observations, the Cu extrusion did not decompose in the following cycles.

Cracking of the particles indicates the presence of tensile stresses in the particles. For the growth of the observed extrusion, several mechanisms may be possible. If stresses are the responsible driving force, then compressive stresses in the particle could account for the extruding material. Based on the results that extrusion and crack were formed at different cell voltages, the SEM observations indicate that Cu substitution by lithium and the further lithium insertion induces different stress fields in the host material. Cu(+) is first reduced to Cu(0) during the early stage of discharge. A volume expansion is expected due to the lithium insertion and the simultaneous presence of Cu. If this volume change is limited by the host structure, compressive stresses could be induced in the particle, which extrude deformable materials such as Cu deposition from the host structure. Further lithium insertion would cause the reduction of Cr(+3.5) and Se(-2), which could result in a straining of the lattice or the formation of a lithium rich phase.

5.1.2 SnO_2

Sn metal has a large capacity for storing lithium by the formation of Li-Sn alloy.[63] However the associated large volume changes during alloying and dealloying lead to rapid capacity fading. For this reason, SnO_2 is used instead as the starting material in the electrode of the lithium-SnO_2 cell. During the first lithium insertion, Li_2O and Sn are formed.[63] If this reaction occurs homogenously, small Sn sub-particles distribute finely in the amorphous Li_2O

matrix. This structure could help to improve the cycle stability during lithium alloying and dealloying in Sn. Therefore, the microstructure formed during the first lithium insertion in SnO_2 particles decides the cycle stability of the electrode.

SnO_2 powder with broad size dispersion was used to build SnO_2-lithium test cells. The microstructural changes of these SnO_2 particles induced by lithium insertion were investigated by means of SEM. A SnO_2-lithium Swagelok-cell was discharged galvanostatically from 3 V to 0.3 V. At 0.75 V (after the second stage in Figure 35) and 0.3 V (after the third stage in Figure 35), several SnO_2 particles on the electrode were imaged by SEM. Comparing the images of these particles before lithium insertion, after the second stage and after the third stage of the first lithium insertion, it can be seen that the particles expanded continuously during the first discharge and there were materials extruded from the particles. The extrusion occurred only during the second stage and in the particles with sizes larger than several hundred nanometers.

More details of the microscopic morphological processes occurring in the electrodes have been identified in the *in situ* SEM observations. Similar changes such as volume changes and extrusions were also found on SnO_2 electrodes in the *in situ* battery experiment. However, the reaction of SnO_2 was found to depend on particle size. Particles with dimensions larger than a few hundred nanometers showed smaller amounts of expansion than the smaller particles. When comparing the SnO_2 particle in Figure 39a with the particle in Figure 39b it can be seen that although the volume expansion is visible, the appearance and shape of the particle surface did not significantly change. This is surprising, since the amount of SnO_2 that is available in the particle must be conserved. If the particle still consists of SnO_2, strains on the order of 25% are required for a volume expansion by a factor of two. Assuming an elastic modulus of 100 GPa[76] this would result in a very high tensile stress of 25 GPa. It is not very likely that the particle can withstand such high stresses since it most likely contains defects such as surface irregularities that may serve as nucleation sites for cracks. It is therefore quite likely that the particle either consists of a material other than SnO_2 or that it is a mixture containing both SnO_2 plus an additional phase. For the case of reactions between SnO_2 and lithium, the formations of Li_2O and Li_xSn alloy both lead to significant volume expansion. Concerning the mechanical stresses; there

are clear indications that there are high tensile stresses in the large particles since cracks were commonly found.

Also extrusions were frequently observed to form on the large particles in the second stage of discharge. The mechanism responsible for the growth of extrusions can be complex but in many systems compressive stresses are responsible for extruding material. Figure 40 shows an example where extrusions grew on a particle. In the SEM images the extrusions appear to be brighter than the particles themselves. The images were taken at beam energies of 10keV and contain not only secondary but also backscattered electrons. The number of backscattered electrons that are generated during imaging depends on the average atomic number of the material under investigation and therefore brighter regions correspond to elements with larger atomic number. Therefore these extrusions could be composed of Sn or Sn-Li alloy that is expected to form during the second stage of discharge where Sn(4+) is reduced by lithium. The number of extrusions increased with the number of cycles when the lithium was inserted into the SnO_2. Some of the extrusions grew in size with the number of cycles, others remained unchanged and new extrusions were observed to form in every cycle. The fact that extrusions form only on the larger particles suggests that the chemical reactions there are inhomogeneous and occur internally.

Characteristic differences between small and large particles were also observed for layer formation on the surface. Particles with dimensions smaller than a few hundred nanometers behave differently from the larger particles. As can be seen from Figure 38, the small particles form layers on their surface. Since the shells in the image appear darker than the particles themselves, it is very likely that these shells consist of Li_2O which has been proposed to form during the first lithium insertion. The observations that were made here show that this process is not reversible, i.e. the shells do not shrink upon lithium extraction. The growth of the shells is not completed after the first cycle. It was observed that the shell increased in thickness over several cycles when lithium was inserted. Inside the shells, brighter regions remain. These regions have shapes that are very similar to the initial particles. Over the course of three cycles, the thickness of the shells significantly increased and the brighter regions slightly decreased in size. This is consistent with the Li_2O formation where the loss in oxygen from the SnO_2 causes a

small volume change in the $Sn+SnO_2$ particle and a large volume change in the Li_2O which is an amorphous low density material. The results indicate that the small SnO_2 particles with dimensions on the order of 100nm form a layer of Li_2O that completely encapsulates the particle as a whole. The volume expansion in this system is solely caused by the formation of the shells and only little volume change in the form of particle shinkage occurs in the core of this composite system. No defects in the form of cracks or extrusions were found on the small particles. It seems that the core-shell composite that forms is effective in reducing the mechanical damage of the particles.

The difference in behavior between small and large particles could be caused by the different reaction kinetics. For a given rate of cycling, there could be a critical particle size where lithium would not reach the SnO_2 inside the particle anymore. As a result, a different behavior is observed.

The fact that the large particles often contain defects in the form of cracks and extrusions suggests that electrodes made from coarse particles are less reliable than electrodes containing only small particles with sizes of 100 nm or below. This conclusion agrees well with electrochemical measurements in the literature.[64,77]

5.2 Intercalation materials

5.2.1 $LiMn_{1.95}Al_{0.05}O_4$

Electrical measurements

The incremental capacity analysis (ICA) helps to understand results of the electrical measurements. A plot of IC versus the corresponding voltage reveals the charge that is needed for changing voltage (dQ/dV) of an electrochemical cell. In this work, each test cell was electrically cycled at a constant rate of 1C (Figure 23). As a result, the electrochemical reaction took place with a constant rate. The ICA of the test cell shown in Figure 23 is illustrated in Figure 45, where two peaks could be identified in every charge or discharge of the lithium-LMAO cell. They correspond to the lithium intercalation at 4 V and the phase transformation at 4.1 V. According to the nature of these two reactions, the low voltage peak is broad and the high voltage peak is quite narrow. Due to the reaction kinetics and the impedance of the test cell, the peak value and the width of the peak depend on the cycling conditions. The peaks were observed at voltages higher than the OCV plateau during charge and at voltages lower than the OCV plateau during discharge. The capacities of the positive electrode can be calculated by integrating the IC curves.

During galvanostatical cycling, the IC curve varied continuously with the cycle number (Figure 45). Several changes could be determined by comparing the IC curves of the 20^{th} cycle and those of the 100^{th}, 300^{th}, 600^{th} and 800^{th} cycle. First of all, both IC peaks move to higher voltage ranges during charge and are shifted to the lower voltage range during discharge. The peak shifts reveal rising ohmic resistance of the test cell and lower the energy conversion efficiency, since more energy is needed for charging the cell, while less energy is released during discharging. The differences of the voltage values between the two peaks are almost unchanged during charge or discharge. Additionally, IC values of each peak decrease with increasing cycle number. The IC value of the high voltage peak during discharge drops more deeply than the others. The integrals of the IC curve over the whole voltage range during charge and discharge are reduced with increasing cycle number. Based on these analyses, a continuous capacity fade

could be identified. These interpretations indicate a degradation of the lithium-LMAO cell in form of increasing resistance and decreasing capacity, which are consequences of different chemical and physical processes occurring on materials inside the cell. The microscopic observation on working electrodes reveals local material changes induced during these processes.

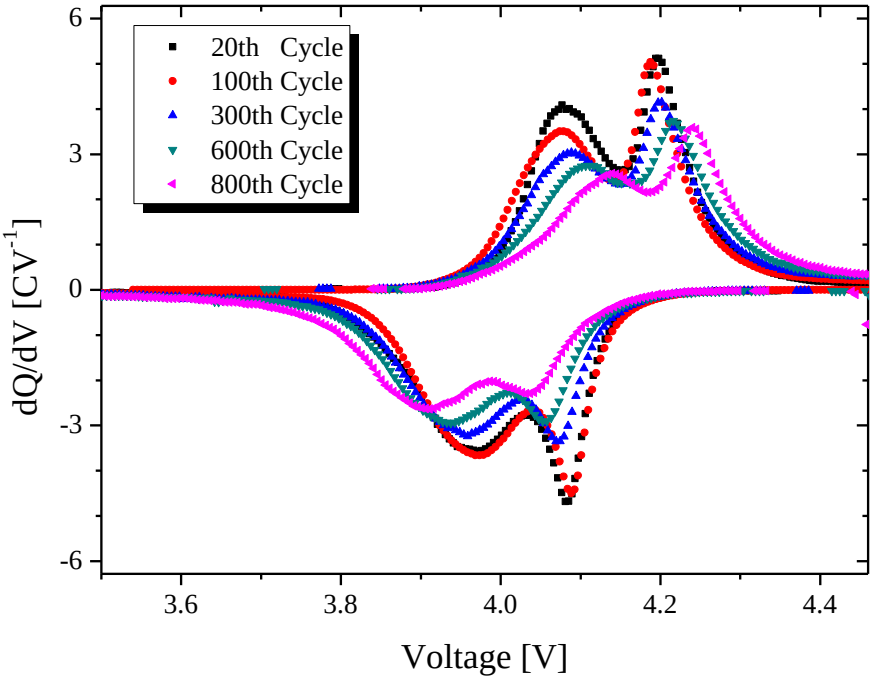

Figure 45: ICA of the LMAO-lithium cell shows electrical degradation with increasing cycle number.

Microscopic observation

Reversible electrochemical lithium ion insertion/extraction into/from host lattices enables lithium storage in the intercalation materials. This process leads to valence changes of transition metals during either lithium intercalation into a single phase with changing lattice parameters or a phase transformation between a lithium rich phase and a lithium poor phase. In both cases, strains are expected inside the particle.

Although the detailed structural response of LMAO to lithium insertion and extraction is not known yet, from data obtained on LMO it can be assumed that there are regions where two phases coexist and that there is a region where insertion/extraction into/from a single phase occurs. Most likely the strains during lithium insertion/extraction lead to the observed degradation of the particle binder interface (Figure 24). One possibility is that the particles "breathe" during battery operation and that the binder has sufficient viscosity to move away from the particles. This effect is a potential degradation path since it lowers the electronic conductivity between active material and current collector.

Also the cracks found inside the LMAO are caused by these strains. In order to form cracks, tensile stress components are needed. Irrespective to the details of the insertion process, stresses will be induced in LMAO particle due to mismatch strain as a result of inhomogeneous lithium intercalation. These stresses are expected since lithium concentration gradients or coexistence of two phases are always associated with gradients of the externally stress free particle which lead to tensile and compressive regions inside the particle. The concentration gradients and the stress distribution are expected to be different during charge and during discharge. Under the assumption that lithium insertion leads to a volume expansion which is the case for most electrode materials, tensile stresses will form in the centre of the particles of the positive electrode during discharge and on the perimeter of the particle during charge.[9-11] The observation in Figure 25 shows crack nucleation and growth during charge as well as during discharge. In the particles, cracks appear on the surface and in the centre as can be seen in Figure 28c.

When larger areas were inspected, it was found that large particles have a much larger probability for developing a crack (Figure 30). Several mechanisms may explain this phenomenon. One argument that could explain particle size dependence is the mechanics of fracture itself. During crack growth, stored elastic energy is transferred into surface energy. This energy balance is different for particles of different size: The elastic energy scales with the three dimensional volume ($\sim r^3$) of a particle whereas the surface energy of the crack surface scales with the two dimensional cross sectional area ($\sim r^2$) of the particle. For a given stress, only particles above a certain size contain enough energy for creating the surface that a crack requires. This energy balance only sets a lower limit for particle size for which crack growth becomes possible. Typically much higher energies are needed to nucleate and advance a crack. Fracture is a process that is affected by defects. At these defects the energetic barrier for generating a crack can be lowered. From brittle bulk materials it is known that the number and size of pre-existing cracks determines the mechanical strength. Applying this concept to small particles leads to the conclusion that for a given defect density, smaller particles are stronger since on average they would contain fewer and smaller defects.

Besides arguments that are concerned with the crack nucleation and growth, the mechanical loading on particles of different size may be considered. During lithium insertion and extraction, concentration profiles will form in the particles. If lithium diffusion through the bulk is the rate limiting step, small particles will have more uniform lithium concentrations than large particles, leading to larger stresses in the larger particles. Okumara et al. determined the diffusivity of lithium in LMO by TOF-SIMS measurements to be 1.23×10^{-15} m^2/s at room temperature.[23,78] With this value a diffusion length of 4.2 µm is obtained after one hour. Although this diffusion length is determined by solving Fick's laws for an infinitely long rod it may be used as an estimate for the characteristic length of the diffusion profile inside the LMAO particles. Particles with lengths smaller than the diffusion length will have smaller lithium concentration gradients and also smaller stresses than larger particles. The maximum stresses inside particles are expected to occur in particles that are equal or larger than the diffusion length. This consideration delivers values of the right order of magnitude and is in agreement with the observation that the probability of finding cracks decreases for particles smaller than roughly 2 µm.

For higher rates, a different particle size distribution should result. In order to investigate these experiments were performed at 3C rate which should shift the particle size distribution by $\sqrt{3}$. In this experiment a similar size distribution was obtained as in the experiment run at 1C. The slightly higher values at 2 µm particle size are statistically not significant.

Altogether there are several reasons that can lead to particle size dependence. Besides different levels of stress due to different lithium concentration distributions, the strength of particles and the energetics of fracture for particles of different size may play a role. For the data presented in Figure 30, it is not unlikely that a superposition of these effects leads to the observed size dependence.

In a brittle material, the atomistic process of forming and growing a crack is deterministic. When stresses and strains oscillate at constant amplitude, cracks should either form during the first cycle or should not appear at all. This is not what was observed here where the number of fractured particles increased with increasing cycle number (Figure 30). This behaviour bears resemblance to what is called fatigue and is different from aging where no cyclic loading occurs. The reason for the nucleation and growth of the cracks must be due to the cyclic electrochemical or mechanical load. In metals, fatigue occurs after a given number of cycles at a given load. Higher loads lead to shorter lifetimes and the relationship between stress/strain amplitude and number of cycles to failure is characterized by the so called SN curve. In highly brittle solids with strong covalent or ionic bonds, fatigue normally does not occur. In brittle solids where dislocations exist, fatigue can occur.[79] In this case, just as in metals, the damage is mediated by the motion of dislocations which pile up at obstacles. If the stored energy in the pile-up is high enough, the energy is released by the nucleation of a crack. The arguments that were discussed before for the particle size dependence of the probability of fracture may also be applied for this fatigue problem. In particular the different stresses that may occur in particles of different size due to different concentration profiles can explain the different stress amplitudes that are active on particles of different size. For some metals, fatigue limits are known to exist, this means that below certain loads no damage is found. A similar effect may exist here, where no damage forms in the smallest particles. There could be an optimum size for preventing particle damage induced by the mechanical stresses and to slow down the chemical side reactions by limiting the solid

electrolyte interface area. The capacity fading of the nano-particles due to the surface layer formation can be minimized in this way too. For these reasons, modification of particle size and their distribution is important to enhance the long-term stability.

A necessary condition for intrinsic fatigue is the existence of dislocations. The bands that can be seen in Figure 27(b, c, and d) and Figure 28a are quite likely slip steps that formed by dislocation gliding to the surface. The result is a sheared crystal as can be seen in Figure 27d. The bands on the front and the top of the particle in Figure 27b may be used to visualize the active glide plane. The location of this plane seems to be parallel to one of the facets of the particle which is suggestive for {111} as being the active glide plane. The fact that dislocation pile-ups are leading to cracks is supported by the fact that many cracks are located in the proximity (Figure 27c) or at the intersection of slip bands (Figure 28a). In disaccord with this description is the fact that before 200 cycles no shear bands were detected in the particles. One possibility is that the dislocations have not reached the particle surface but still pile-ups had occurred inside the particle. Another possibility is that a different fatigue or damage mechanism was active.

The aforementioned arguments are of purely mechanical nature. In this work, damage was observed to form with increasing numbers of cycles. Such fatigue phenomena cannot be easily explained in brittle, ceramic materials. Two arguments are suggested considering the electrochemical conditions in the lithium-ion battery. Once defects, such as dislocations and cracks exist, the local stoichiometry is modified and a locally different electrochemical response can be expected. Most likely, the changes in stoichiometry have a negative effect on the capacity of an electrode material. At a dislocation or at a crack tip less lithium can be inserted/extracted than in the defect free regions. Consequences of this effect are modified stress profiles around a defect that depend on the state of charge and that may lead to the motion or growth of a defect during cycling. Another argument that may be considered is the extreme electrochemical conditions that are active. At the defects effects as observed in stress corrosion cracking could be active. The local stress (σ) at the crack tip and the fracture toughness (K_c) at the corrosion region could be changed due to the two mechanisms mentioned above. In case of increased local stress or lowered fracture toughness, crack growth may be activated at the crack tip without significant

dislocation motion. The rate of such kind of crack growth is limited due to the time limiting step, in this case, the corrosion process or the lithium diffusion in the solid material. As a result, a brittle frature would not take place until the critical crack length (a_c) is reached, in which the released energy by cracking is larger than the surface energy. This subcritical crack growth mechanism may explain the fatigue of the single crystaline brittle particles under cyclic load and electrochemical conditions in the lithium-ion battery.

For many brittle materials, a sigmoidal variation is typically observed by double logarithmic plotting of the rate of fatigue crack growth (da/dN) against stress intensity factor range (ΔK) (Figure 46). An increase of the subcritical crack growth rate can be observed in region *I*, which is mathematically expressed by formula 1 (Paris law). The stress intensity factor range is given by the stress amplitude and the crack length (a) as shown in formula 2. In the studied case in this work, particles with the same size were cycled under contant load $\Delta\sigma$, ΔK increases with increasing crack length *a*, which accelerates the crack growth. After reaching the critical crack length in region *II*, fracture occurs in the brittle particles. In the same electrode, the periodic load $\Delta\sigma$ in the large particles were larger than that in the small particles. As a result, the Paris exponent *n* (formula 1) for the large particles is higher than the one for the small particles. According to the formula 2, the critical crack lengths for the large particles are smaller. This fatigue mechanism agrees to the relationship between the fracture rate and the particles size observed in the experiment (Figure 30).

$$da/dN = A(\Delta K)^n \qquad \text{(Formula 1)}$$

$$\Delta K \sim a^{-1/2}\Delta\sigma \qquad \text{(Formula 2)}$$

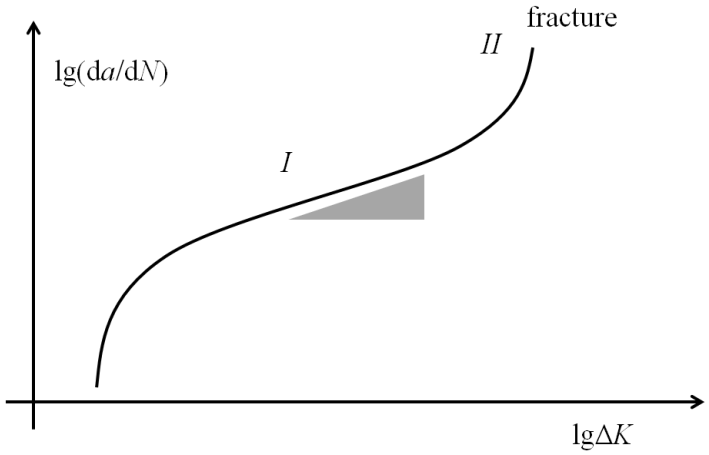

Figure 46: A typical devolution of the rate of fatigue crack growth over the stress intensity factor range (ΔK) of brittle material under cyclical load. Region *I*: subcritical crack growth, region *II*: critical crack growth and fracture.

The effect of cracks on the capacity of an electrode is often debated. Advantageous for the battery performance is that cracks enhance the surface to volume ratio of the active material. For LMAO, the additional surfaces are quite likely {111} planes and their behavior should be similar to other {111} surfaces on the particles. Disadvantageous is the fact that mechanical damage such as dislocations and cracks can lead to a loss of electronic and ionic conductivity. This is particularly the case when multiple cracks run inside one particle as can be seen in Figure 28c and regions of the particle are electronically disconnected from their surroundings. As a result, capacity fading and resistance increase were detected in the electrical measurement by analyzing the incremental capacity.

How much capacity fading is due to cracks is very hard to assess. A rather crude attempt can be made using the data from Table 4, Table 5 and Table 6. After 800 cycles the total volume of particles detected by SEM is 590 μm^3 and the total volume of the particles with cracks is 297 μm^3. If a cracked particle loses all of its capacity this would cause a loss of 50% in capacity. In order to obtain the measured 23% capacity loss, 46% of the volume of the cracked particles is inactive and 54% is still active. This consideration is only valid if the full capacity loss is due to

mechanical damage. For the case that additional degradation mechanisms are simultaneously active, more than 54% of the capacity is retained in the fractured particles. When looking at Figure 28c it seems that in some cases a significant volume fraction of the particles can be lost. This indicates that a considerable part of the measured capacity loss may be due to mechanical damage.

When the symmetry of the cracks was observed (Figure 28b), it was found that many particle surfaces are {111} planes. This information has been observed before on larger LMO single crystals [80] and may be helpful in obtaining a better understanding of the insertion process where knowledge of the surface orientation is critical. The fact that the particles have {111} surfaces is surprising because according to density functional theory (DFT) calculations these orientations, independent of their detailed atomic termination, have relatively high surface and cohesive energies as compared to {100} and {110} orientations.[81] Depending on the synthesis route, thermodynamics may not be the factor that determines the surface orientation, it could also be the case that diffusion anisotropy or nucleation limitations lead to the selection of the {111} surface as the growth direction for the particles. In terms of the energies determined by DFT it is also surprising that most of the observed cracks run on {111} planes. This is an effect that may be associated with the orientation dependence of dislocations in this cubic crystal.

5.2.2 $LiCoO_2$ and $LiNi_{0.4}Fe_{0.1}Mn_{1.5}O_4$

LCO was cycled at 1C rate for 220 cycles between 3.5V and 4.2V. No mechanical damage was observed on the particle surface after that. Due to the high coefficient for lithium, the lithium concentration gradient in the LCO solid phase is expected to be smaller than that in the manganese spinel. Moreover the smaller volume change during charge/discharge of LCO reduces further the mismatch in the particles. As a result, the stresses induced in the LCO are expected to be smaller than that of the manganese spinel and LMAO spinel particles. The observation of LCO indicates the critical role of the amplitude of cyclic mechanical loads in initiating cracks.

LMNFO spinel was also investigated in this study. An *ex situ* cell with LMNFO electrode was cycled with 2C rate for 986 cycles between 3.5 V and 5 V. No crack or other morphological change was observed on the particles. Similar to LCO, the fast lithium and electron transport in the LMNFO reduce the stresses formed during lithium de-/intercalation. Additionally, the Fe enrichment at the surface helps to form protective layers between solid particles and liquid electrolyte, which slow down the interface corrosion and therefore inhibits the crack initiation. Both effects protect LMNFO from mechanical damage even with very high cycle numbers as shown in this work. The robustness enables a wide usage of this material in applications which require a high cyclic stability, and especially at low temperatures, where the lithium diffusivity is greatly reduced.

6 Summary

In this work, electrode materials for lithium-ion batteries have been investigated in an SEM. A technique for *in situ* SEM observation was developed and used for the first time and additional experiments were performed using an *ex situ* SEM method that allows for the comparison of the same location before, during and after electrochemical tests. This technique is particularly useful for experiments at higher cycle numbers. Both methods exhibit a spatial resolution of ~1nm which is unprecedented in the research of secondary batteries, where volume averaging techniques are typically employed. In this thesis, both experimental methods were applied to electrode materials for the first time. Irrespective of the individual material, it became evident that in electrode materials for lithium-ion batteries mechanical effects are very pronounced. This is of particular importance for current and future conversion materials where large amounts of lithium are inserted and extracted and large volume expansions are expected. Also conventional intercalation/insertion materials have been observed to be affected by stresses and suffer from mechanical degradation.

Reaction pathways were investigated in conversion materials. For $CuCr_2Se_4$ a combined mechanism of a conversion and insertion reaction was observed. This happened together with *in situ* synchrotron x-ray measurements. Here the SEM observations proved useful for revealing the formation of Cu extrusions at early stages of lithium insertion. In the SEM measurement the enormous volume expansions and the formation and growth of cracks in this system became apparent, suggesting a poor reversibility of the processes in this material. In SnO_2, a two stage process that was proposed in the literature was confirmed. First Li_2O is formed and during further reaction with lithium, an alloy between lithium and tin forms. It could be shown, that the first step is irreversible and that for the second step a particle size dependence occurs, where small particles are encapsulated by a layer presumably consisting of Li_2O. Large particles do not seem to show this layer but their volume expansion is suggestive of a formation of Li_2O inside the particles. Since Li_2O prevents particles from tin agglomeration and may help to reduce the volume expansion, a better reliability of SnO_2 with small particle sizes is expected.

Investigations in intercalation materials were performed up to 800 cycles. The main focus of this thesis was on LMAO, a material that is already used in large scale applications. It was found that for this material, mechanical effects are of crucial importance. It was found that particles can crack due to repeated reaction with lithium. This process of crack formation and growth seems to have two components. One is due to brittle failure and another one is caused by mechanical fatigue. Again a dependence of particle size was found, where small particles were significantly more resistant against damage. Different underlying mechanisms may be causing these mechanical effects and have been discussed. A possible candidate is the mechanical stresses that are due to the lithium insertion kinetics. Lithium transport inside particles takes time and when lithium is inserted or extracted, lithium concentration gradients will form, leading to stress gradients in the particles. According to this, at a given rate, large particles have larger gradients and therefore are more susceptible to damage. For the rate of 1C which was used here no significant damage was found in particles with sizes below 200nm. This description is in agreement with the fact that no mechanical damage was found on LCO and LMNFO, where the lithium diffusivity is at least one order of magnitude higher. Although cracks create additional surface area in an electrode and are sometimes even discussed to be beneficial for a battery, it could be shown in this thesis, that large particles can be disconnected and that this could easily lead to a capacity loss as the one observed here which was ~25% after 800 cycles.

Mechanical effects need to be considered in high capacity conversion materials where large volume expansions have to be expected. As can be seen in this thesis mechanical stresses also need to be critically assessed in insertion or intercalation materials. There processes such as mechanical fatigue can occur. In particular the data acquired on LMAO is of technological importance and needs to be considered for systems where long term reliability is of importance. Altogether, the observations and interpretation presented in this work fortify the importance of mechanical effects for lithium-ion batteries and may prove to be helpful for designing batteries with better reliability in the future.

7 Acknowledgment

Die vorliegende Doktorarbeit wurde in der Zeit zwischen 2008 und 2011 am Institut für Angewandte Materialien vom Karlsruher Institut für Technologie angefertigt.

Herrn Prof. Dr. O. Kraft danke ich für die Stellung dieser Promotion in seinem Institut sowie sein stets Interesse an der Arbeit und viele hilfreiche Anregungen, die zum Gelingen der Arbeit ermöglicht haben. Desweiteren danke ich Herrn Prof. Dr. M. Karmlah, der mir eine gute Zusammenarbeit mit anderen Doktoranden in der Abteilung ermöglicht hat. Herrn Prof. Dr. M. Hoffmann danke ich für die freundliche Übernahme des Mitberichts.

Mein besonderer Dank gilt meinem Betreuer Dr. R. Mönig, der mich den Zugang in das Fachgebiet ermöglichte und stets bereit war, vor Probleme mitzuhelfen. Dr. S. Indris verdanke ich für die freundliche Zusammenarbeit und den tiefen Einblick in die Batteriethematik. Für die Hilfen, Anregungen und Diskussionen aller Arten bin ich die Freunden und Kollegen in der Arbeitsgruppe S. Schendel, A. Sedlmayr, Dr. Z. Choi, Dr. S. Boles, Dr. D. Gianola und mein Bürokollege T. Neidthardt herzlich dankbar. Natürlich gilt auch mein Dank allen Kollegen im Umfeld des IAMs und INTs, die mich während meiner Arbeit unterstützt haben und für die angenehme Arbeitsatmosphäre besorgt haben.

8 References

1. Tarascon, J.M. & Guyomard, D. The $Li_{1+X}Mn_2O_4$/C Rocking-Chair System - a Review. *Electrochimica Acta* **38**, 1221-1231 (1993).
2. Tarascon, J.M. & Armand, M. Issues and challenges facing rechargeable lithium batteries. *Nature* **414**, 359-367 (2001).
3. Vetter, J., Novak, P., Wagner, M.R., Veit, C., Moller, K.C., Besenhard, J.O., Winter, M., Wohlfahrt-Mehrens, M., Vogler, C. & Hammouche, A. Ageing mechanisms in lithium-ion batteries. *Journal of Power Sources* **147**, 269-281 (2005).
4. Spotnitz, R. Simulation of capacity fade in lithium-ion batteries. *Journal of Power Sources* **113**, 72-80 (2003).
5. Arora, P., White, R.E. & Doyle, M. Capacity fade mechanisms and side reactions in lithium-ion batteries. *Journal of the Electrochemical Society* **145**, 3647-3667 (1998).
6. Broussely, M., Biensan, P., Bonhomme, F., Blanchard, P., Herreyre, S., Nechev, K. & Staniewicz, R.J. Main aging mechanisms in Li ion batteries. *Journal of Power Sources* **146**, 90-96 (2005).
7. Markovsky, B., Rodkin, A., Cohen, Y.S., Palchik, O., Levi, E., Aurbach, D., Kim, H.J. & Schmidt, M. The study of capacity fading processes of Li-ion batteries: major factors that play a role. *Journal of Power Sources* **119**, 504-510 (2003).
8. Aurbach, D., Markovsky, B., Rodkin, A., Levi, E., Cohen, Y.S., Kim, H.J. & Schmidt, M. On the capacity fading of $LiCoO_2$ intercalation electrodes: the effect of cycling, storage, temperature, and surface film forming additives. *Electrochimica Acta* **47**, 4291-4306 (2002).
9. Cheng, Y.T. & Verbrugge, M.W. Diffusion-Induced Stress, Interfacial Charge Transfer, and Criteria for Avoiding Crack Initiation of Electrode Particles. *Journal of the Electrochemical Society* **157**, A508-A516 (2010).
10. Cheng, Y.T. & Verbrugge, M.W. Application of Hasselman's Crack Propagation Model to Insertion Electrodes. *Electrochemical and Solid State Letters* **13**, A128-A131 (2010).

11. Deshpande, R., Cheng, Y.T., Verbrugge, M.W. & Timmons, A. Diffusion Induced Stresses and Strain Energy in a Phase-Transforming Spherical Electrode Particle. *Journal of the Electrochemical Society* **158**, A718-A724 (2011).
12. Garcia, R.E., Chiang, Y.M., Carter, W.C., Limthongkul, P. & Bishop, C.M. Microstructural modeling and design of rechargeable lithium-ion batteries. *Journal of the Electrochemical Society* **152**, A255-A263 (2005).
13. Renganathan, S., Sikha, G., Santhanagopalan, S. & White, R.E. Theoretical Analysis of Stresses in a Lithium Ion Cell. *Journal of the Electrochemical Society* **157**, A155-A163 (2010).
14. Wang, H.F., Jang, Y.I., Huang, B.Y., Sadoway, D.R. & Chiang, Y.M. Electron microscopic characterization of electrochemically cycled $LiCoO_2$ and $Li(Al,Co)O_2$ battery cathodes. *Journal of Power Sources* **81**, 594-598 (1999).
15. Gabrisch, H., Yazami, R. & Fultz, B. The character of dislocations in $LiCoO_2$. *Electrochemical and Solid State Letters* **5**, A111-A114 (2002).
16. Christensen, J. & Newman, J. Stress generation and fracture in lithium insertion materials. *Journal of Solid State Electrochemistry* **10**, 293-319 (2006).
17. Christensen, J. & Newman, J. A mathematical model of stress generation and fracture in lithium manganese oxide. *Journal of the Electrochemical Society* **153**, A1019-A1030 (2006).
18. Christensen, J. Modeling Diffusion-Induced Stress in Li-Ion Cells with Porous Electrodes. *Journal of the Electrochemical Society* **157**, A366-A380 (2010).
19. Zhang, X., Shyy, W. & Sastry, A.M. Numerical simulation of intercalation-induced stress in Li-ion battery electrode particles (vol 154, pg A910, 2007). *Journal of the Electrochemical Society* **154**, S21-S21 (2007).
20. Zhang, X.C., Sastry, A.M. & Shyy, W. Intercalation-induced stress and heat generation within single lithium-ion battery cathode particles. *Journal of the Electrochemical Society* **155**, A542-A552 (2008).
21. Zhao, K.J., Pharr, M., Vlassak, J.J. & Suo, Z.G. Fracture of electrodes in lithium-ion batteries caused by fast charging. *Journal of Applied Physics* **108**(2010).

22. Woodford, W.H., Chiang, Y.M. & Carter, W.C. "Electrochemical Shock" of Intercalation Electrodes: A Fracture Mechanics Analysis. *Journal of the Electrochemical Society* **157**, A1052-A1059 (2010).
23. Reimers, J.N. & Dahn, J.R. Electrochemical and Insitu X-Ray-Diffraction Studies of Lithium Intercalation in $LixCoO_2$. *Journal of the Electrochemical Society* **139**, 2091-2097 (1992).
24. Ohzuku, T. & Ueda, A. Solid-State Redox Reactions of $LiCoO_2$ (R(3)over-Bar-M) for 4 Volt Secondary Lithium Cells. *Journal of the Electrochemical Society* **141**, 2972-2977 (1994).
25. Amatucci, G.G., Tarascon, J.M. & Klein, L.C. CoO_2, the end member of the Li_xCoO_2 solid solution. *Journal of the Electrochemical Society* **143**, 1114-1123 (1996).
26. Van der Ven, A., Aydinol, M.K. & Ceder, G. First-principles evidence for stage ordering in Li_xCoO_2. *Journal of the Electrochemical Society* **145**, 2149-2155 (1998).
27. Mizushima, K., Jones, P.C., Wiseman, P.J. & Goodenough, J.B. Li_xCoO_2 "(Oless-Thanxless-Than-or-Equal-To1) - a New Cathode Material for Batteries of High-Energy Density. *Materials Research Bulletin* **15**, 783-789 (1980).
28. Goodenough, J.B., Mizushima, K. & Takeda, T. Solid-Solution Oxides for Storage-Battery Electrodes. *Japanese Journal of Applied Physics* **19**, 305-313 (1980).
29. Mendiboure, A., Delmas, C. & Hagenmuller, P. New Layered Structure Obtained by Electrochemical Deintercalation of the Metastable $LiCoO_2$ (02) Variety. *Materials Research Bulletin* **19**, 1383-1392 (1984).
30. Mizushima, K., Jones, P.C., Wiseman, P.J. & Goodenough, J.B. Li_xCoO_2 (O Less-Than X Less-Than-or-Equal-to 1) - a New Cathode Material for Batteries of High-Energy Density. *Solid State Ionics* **3-4**, 171-174 (1981).
31. Thomas, M.G.S.R., Bruce, P.G. & Goodenough, J.B. Ac Impedance of the $Li_{(1-X)}CoO_2$ Electrode. *Solid State Ionics* **18-9**, 794-798 (1986).
32. Thackeray, M.M., David, W.I.F., Bruce, P.G. & Goodenough, J.B. Lithium Insertion into Manganese Spinels. *Materials Research Bulletin* **18**, 461-472 (1983).
33. Chen, L.Q. & Schoonman, J. Polycrystalline, Glassy, and Thin-Films of $LiMn_2O_4$. *Solid State Ionics* **67**, 17-23 (1993).

34. Chen, L.Q., Huang, X.J., Kelder, E. & Schoonman, J. Diffusion Enhancement in $Li_xMn_2O_4$. *Solid State Ionics* **76**, 91-96 (1995).

35. Barker, J., Pynenburg, R. & Koksbang, R. Determination of Thermodynamic, Kinetic and Interfacial Properties for the $Li//Li_xMn_2O_4$ System by Electrochemical Techniques. *Journal of Power Sources* **52**, 185-192 (1994).

36. Winter, M., Besenhard, J.O., Spahr, M.E. & Novak, P. Insertion electrode materials for rechargeable lithium batteries. *Advanced Materials* **10**, 725-763 (1998).

37. Eriksson, T., Hjelm, A.K., Lindbergh, G. & Gustafsson, T. Kinetic study of $LiMn_2O_4$ cathodes by in situ XRD with constant-current cycling and potential stepping. *Journal of the Electrochemical Society* **149**, A1164-A1170 (2002).

38. Ohzuku, T., Kitagawa, M. & Hirai, T. Electrochemistry of Manganese-Dioxide in Lithium Nonaqueous Cell .3. X-Ray Diffractional Study on the Reduction of Spinel-Related Manganese-Dioxide. *Journal of the Electrochemical Society* **137**, 769-775 (1990).

39. Chung, K.Y., Lee, H.S., Yoon, W.S., McBreen, J. & Yang, X.Q. Studies of $LiMn_2O_4$ capacity fading at elevated temperature using in situ synchrotron X-ray diffraction. *Journal of the Electrochemical Society* **153**, A774-A780 (2006).

40. Yang, X.Q., Sun, X., Lee, S.J., McBreen, J., Mukerjee, S., Daroux, M.L. & Xing, X.K. In situ synchrotron X-ray diffraction studies of the phase transitions in $Li_xMn_2O_4$ cathode materials. *Electrochemical and Solid State Letters* **2**, 157-160 (1999).

41. Goodenough, J.B., Thackeray, M.M., David, W.I.F. & Bruce, P.G. Lithium Insertion Extraction Reactions with Manganese Oxides. *Revue De Chimie Minerale* **21**, 435-455 (1984).

42. Thackeray, M.M., Depicciotto, L.A., Dekock, A., Johnson, P.J., Nicholas, V.A. & Adendorff, K.T. Spinel Electrodes for Lithium Batteries - a Review. *Journal of Power Sources* **21**, 1-8 (1987).

43. Momchilov, A., Manev, V., Nassalevska, A. & Kozawa, A. Rechargeable Lithium Battery with Spinel-Related MnO_2 .2. Optimization of the $LiMn_2O_4$ Synthesis Conditions. *Journal of Power Sources* **41**, 305-314 (1993).

44. Gummow, R.J., Dekock, A. & Thackeray, M.M. Improved Capacity Retention in Rechargeable 4V Lithium Lithium Manganese Oxide (Spinel) Cells. *Solid State Ionics* **69**, 59-67 (1994).

45. Komaba, S., Oikawa, K., Myung, S.T., Kumagai, N. & Kamiyama, T. Neutron powder diffraction studies of $LiMn_{2-y}Al_yO_4$ synthesized by the emission drying method. *Solid State Ionics* **149**, 47-52 (2002).

46. Myung, S.T., Komaba, S. & Kumagai, N. Enhanced structural stability and cyclability of Al-doped $LiMn_2O_4$ spinel synthesized by the emulsion drying method. *Journal of the Electrochemical Society* **148**, A482-A489 (2001).

47. Dunger, H.J., Hambitzer, G. & Lutter, W. Lithium-Cycling Efficiency in Inorganic Electrolyte Solution. *Journal of Power Sources* **44**, 405-408 (1993).

48. Dreher, J., Haas, B. & Hambitzer, G. Rechargeable $LiCoO_2$ in Inorganic Electrolyte Solution. *Journal of Power Sources* **44**, 583-587 (1993).

49. Hambitzer, G., Joos, M. & Schriever, U. Volatile Products of Electrode-Reactions in Inorganic Electrolyte. *Journal of Power Sources* **44**, 727-732 (1993).

50. Liu, J. & Manthiram, A. Kinetics Study of the 5 V Spinel Cathode $LiMn_{(1.5)}Ni_{(0.5)}O_{(4)}$ Before and After Surface Modifications. *Journal of the Electrochemical Society* **156**, A833-A838 (2009).

51. Manthiram, A. & Liu, J. Functional surface modifications of a high capacity layered $Li[Li_{(0.2)}Mn_{(0.54)}Ni_{(0.13)}Co_{(0.13)}]O_{(2)}$ cathode. *Journal of Materials Chemistry* **20**, 3961-3967 (2010).

52. Wu, Y. & Manthiram, A. High capacity, surface-modified layered $Li[Li_{(1-x)/3}Mn_{(2-x)/3}Ni_{x/3}Co_{x/3}]O_2$ cathodes with low irreversible capacity loss. *Electrochemical and Solid State Letters* **9**, A221-A224 (2006).

53. Wu, Y., Murugan, A.V. & Manthiram, A. Surface modification of high capacity layered $Li[Li_{0.2}Mn_{0.54}Ni_{0.13}Co_{0.13}]O_2$ cathodes by $AlPO_4$. *Journal of the Electrochemical Society* **155**, A635-A641 (2008).

54. Manthiram, A. & Liu, J. Understanding the Improved Electrochemical Performances of Fe-Substituted 5 V Spinel Cathode $LiMn_{(1.5)}Ni_{(0.5)}O_{(4)}$. *Journal of Physical Chemistry C* **113**, 15073-15079 (2009).

55. Liu, J. & Manthiram, A. Understanding the Improved Electrochemical Performances of Fe-Substituted 5 V Spinel Cathode $LiMn_{1.5}Ni_{0.5}O_4$. *Journal of Physical Chemistry C* **113**, 15073-15079 (2009).

56. Guyomard, D. & Tarascon, J.M. High-Voltage Stable Liquid Electrolytes for $Li_{1+X}Mn_2O_4$/Carbon Rocking-Chair Lithium Batteries. *Journal of Power Sources* **54**, 92-98 (1995).

57. Malini, R., Uma, U., Sheela, T., Ganesan, M. & Renganathan, N.G. Conversion reactions: a new pathway to realise energy in lithium-ion battery-review. *Ionics* **15**, 301-307 (2009).

58. Cabana, J., Monconduit, L., Larcher, D. & Palacin, M.R. Beyond Intercalation-Based Li-Ion Batteries: The State of the Art and Challenges of Electrode Materials Reacting Through Conversion Reactions. *Advanced Materials* **22**, E170-E192 (2010).

59. Yamaguchi, Y., Ohishi, Y., Ohashi, M., Yamashita, O. & Watanabe, H. Electric-Conductivity and 3d-Electron Distribution in $CuCr_2Se_{4-X}Br_x$. *Japanese Journal of Applied Physics* **19**, 291-293 (1980).

60. Bodenez, V., Dupont, L., Morcrette, M., Surcin, C., Murphy, D.W. & Tarascon, J.M. Copper extrusion/reinjection in Cu-based thiospinels by electrochemical and chemical routes. *Chemistry of Materials*, 4278-4287 (2006).

61. Bodenez, V., Dupont, L., Laffont, L., Armstrong, A.R., Shaju, K.M., Bruce, P.G. & Tarascon, J.M. The reaction of lithium with $CuCr_2S_4$ - lithium intercalation and copper displacement/extrusion. *Journal of Materials Chemistry*, 3238-3247 (2007).

62. Bensch, W., Ophey, J., Hain, H., Gesswein, H., Chen, D., Mönig, R., Gruber, P.A. & Indris, S. Chemical and electrochemical insertion of Li into spinel structure of $CuCr_2Se_4$: *ex situ* and *in situ* obervation by X-ray diffraction and scanning electron microscopy. *Physical Chemistry Chemical Physics*, 7509 (2012).

63. Courtney, I.A. & Dahn, J.R. Electrochemical and in situ x-ray diffraction studies of the reaction of lithium with tin oxide composites. *Journal of the Electrochemical Society* **144**, 2045-2052 (1997).

64. Yang, J., Winter, M. & Besenhard, J.O. Small particle size multiphase Li-alloy anodes for lithium-ion-batteries. *Solid State Ionics* **90**, 281-287 (1996).

65. Arakawa, M., Tobishima, S., Nemoto, Y., Ichimura, M. & Yamaki, J. Lithium Electrode Cycleability and Morphology Dependence on Current-Density. *Journal of Power Sources* **43**, 27-35 (1993).

66. Osaka, T., Homma, T., Momma, T. & Yarimizu, H. In situ observation of lithium deposition processes in solid polymer and gel electrolytes. *Journal of Electroanalytical Chemistry* **421**, 153-156 (1997).

67. Takehara, Z., Ogumi, Z., Uchimoto, Y., Yasuda, K. & Yoshida, H. Modification of Lithium Electrolyte Interface by Plasma Polymerization of 1,1-Difluoroethene. *Journal of Power Sources* **44**, 377-383 (1993).

68. Aurbach, D., Gofer, Y. & Langzam, J. The Correlation between Surface-Chemistry, Surface-Morphology, and Cycling Efficiency of Lithium Electrodes in a Few Polar Aprotic Systems. *Journal of the Electrochemical Society* **136**, 3198-3205 (1989).

69. Osaka, T., Momma, T., Matsumoto, Y. & Uchida, Y. Surface characterization of electrodeposited lithium anode with enhanced cycleability obtained by CO2 addition. *Journal of the Electrochemical Society* **144**, 1709-1713 (1997).

70. Langenhuizen, N.P.W. The effect of mass transport on Li deposition and dissolution. *Journal of the Electrochemical Society* **145**, 3094-3099 (1998).

71. Baudry, P. & Armand, M. In situ Observation by SEM of positive Composite Electrodes druing Discharge of Polymer Lithium Batteries. *Solid State Ionics* **28-30**, 1567-1571 (1988).

72. Orsini, F., Du Pasquier, A., Beaudoin, B., Tarascon, J.M., Trentin, M., Langenhuizen, N., De Beer, E. & Notten, P. In situ Scanning Electron Microscopy (SEM) observation of interfaces within plastic lithium batteries. *Journal of Power Sources* **76**, 19-29 (1998).

73. Raimann, P.R., Hochgatterer, N.S., Korepp, C., Moller, K.C., Winter, M., Schrottner, H., Hofer, F. & Besenhard, J.O. Monitoring dynamics of electrode reactions in Li-ion batteries by in situ ESEM. *Ionics* **12**, 253-255 (2006).

74. Huang, J.Y., Zhong, L., Wang, C.M., Sullivan, J.P., Xu, W., Zhang, L.Q., Mao, S.X., Hudak, N.S., Liu, X.H., Subramanian, A., Fan, H.Y., Qi, L., Kushima, A. & Li, J. In situ Observation of the Electrochemical Lithiation of a Single SnO_2 Nanowire Electrode. *Science* **330**(2010).

75. Dubarry, M., Svoboda, V., Hwu, R. & Liaw, B.Y. Incremental capacity analysis and close-to-equilibrium OCV measurements to quantify capacity fade in commercial rechargeable lithium batteries. *Electrochemical and Solid State Letters* **9**, A454-A457 (2006).

76. Barth, S., Harnagea, C., Mathur, S. & Rosei, F. The elastic moduli of oriented tin oxide nanowires. *Nanotechnology* **20**, - (2009).

77. Chen, Y.C., Chen, J.M., Huang, Y.H., Lee, Y.R. & Shih, H.C. Size effect of tin oxide nanoparticles on high capacity lithium battery anode materials. *Surface & Coatings Technology* **202**, 1313-1318 (2007).

78. Okumura T., F.T., Uchimoto Y., Sakai N., Yamaji K., Yokokawa H. Determination of lithium ion diffusion in lithium-manganese-oxide-spinel thin films by secondary-ion mass spectrometry. *Journal of Power Sources* **189**, 643-645 (2009).

79. Forsyth, P.J.E. Slip band damage and extrusion. *Proceedings of the Royal Society* **A242**, 198-202 (1957).

80. Akimoto J., T.Y., Gotoh Y., Mizuta S. Single crystal growth of the spinel-type $LiMn_2O_4$. *Journal of Crystal Growth* **229**, 405-408 (2001).

81. Benedek, R. & Thackeray, M.M. Simulation of the surface structure of lithium manganese oxide spinel. *Physical Review B* **83**(2011).